



**HAL**  
open science

# Transforming Cobalt Nanospheres into Co<sub>2</sub>P Nanorods: The Key Roles of Oleylamine and Organophosphorus Ligands in Co(I) Precursor Uncovered Through XPS Analysis

Rabah Benbalagh, François Rochet, Arthur Moisset, Alexandre Sodreau,  
Cassandre Bories, Caroline Salzemann, Christophe Petit, Marc Petit

## ► To cite this version:

Rabah Benbalagh, François Rochet, Arthur Moisset, Alexandre Sodreau, Cassandre Bories, et al.. Transforming Cobalt Nanospheres into Co<sub>2</sub>P Nanorods: The Key Roles of Oleylamine and Organophosphorus Ligands in Co(I) Precursor Uncovered Through XPS Analysis. *Journal of Physical Chemistry C*, 2024, 128 (8), pp.3408-3422. 10.1021/acs.jpcc.3c08365 . hal-04446428

**HAL Id: hal-04446428**

**<https://hal.science/hal-04446428>**

Submitted on 8 Feb 2024

**HAL** is a multi-disciplinary open access archive for the deposit and dissemination of scientific research documents, whether they are published or not. The documents may come from teaching and research institutions in France or abroad, or from public or private research centers.

L'archive ouverte pluridisciplinaire **HAL**, est destinée au dépôt et à la diffusion de documents scientifiques de niveau recherche, publiés ou non, émanant des établissements d'enseignement et de recherche français ou étrangers, des laboratoires publics ou privés.

## **Transforming Cobalt Nanospheres into Co<sub>2</sub>P Nanorods: The Key Roles of Oleylamine and Organophosphorus Ligands in Co(I) Precursor Uncovered Through XPS Analysis**

*Rabah Benbalagh<sup>1</sup>, François Rochet<sup>1\*</sup>, Arthur Moisset<sup>2</sup>, Alexandre Sodreau<sup>3</sup>, Cassandre Bories<sup>3</sup>, Caroline Salzemann<sup>2</sup>, Christophe Petit<sup>2</sup> and Marc Petit<sup>3</sup>*

<sup>1</sup>Sorbonne Université, CNRS, Laboratoire de Chimie Physique – Matière et Rayonnement, UMR 7614, 4 place Jussieu, 75005 Paris, France

<sup>2</sup>Sorbonne Université, CNRS, MONARIS, UMR 8233, 4 place Jussieu, 75005 Paris, France.

<sup>3</sup>Sorbonne Université, CNRS, Institut Parisien de Chimie Moléculaire, UMR 8232, 75005 Paris, France.

\*Corresponding author: [francois.rochet@sorbonne-universite.fr](mailto:francois.rochet@sorbonne-universite.fr)

### **Abstract:**

This research offers fresh insights into the growth mechanism of cobalt nanoparticles in oleylamine from a precursor with nominal stoichiometry  $\text{CoCl}(\text{PPh}_3)_3$ , prompting a reevaluation of the model delineated in "*The five Shades of Oleylamine*" by Moisset *et al.* (*Nanoscale* **2021**, *13*, 11289–11297) that explicated the cobalt sphere-to-rod morphological transition. While the crucial role of oleylamine is reconfirmed, X-ray photoelectron spectroscopy (XPS) discloses the significant involvement of the organophosphorus ligand of the Co(I) precursor. By scrutinizing aliquots from a tetradecane:oleylamine solution, XPS substantiates the disproportionation of Co(I) into Co(II) and  $\text{Co}^\circ$  during the sphere growth stage in line with the tenets of *Five Shades*. Pure Co spheres are formed, with phosphorus-containing species disappearing from the XPS probed layers. However, further inspection of washed nanoparticles corroborates the formation of Co-P bonds, with the Co/P atomic ratio nearing 2

for the nanorods. In response to these findings, previously published data and electron diffraction patterns of the nanorods structure are reassessed, conclusively demonstrating that the nanorods are composed of  $\text{Co}_2\text{P}$ , contrary to earlier assumptions of pure cobalt content. This leads to a revised depiction of the sphere-to-rod transition, placing emphasis on the role of organophosphorus ligands (triphenylphosphine and, possibly, its oxidation products) that were previously overlooked.

## 1. Introduction

Hexagonal close-packed (hcp) cobalt nanoparticles have garnered significant scientific interest owing to their catalytic properties<sup>1,2</sup> and high magnetocrystalline anisotropy,<sup>3</sup> rendering them suitable for the fabrication of magnetic devices. In contrast to other synthesis pathways explored so far, such as the reduction of inorganic  $\text{Co(II)}$  or  $\text{Co(III)}$  complexes,<sup>4</sup> or the decomposition of dicobaltoctacarbonyl molecule,<sup>5</sup> the use of the  $\text{Co(I)Cl(P(C}_6\text{H}_5)_3)_3$  precursor has emerged as a highly promising procedure to produce nanoparticles with very well controlled shape and size.<sup>6,2</sup>

However, when oleylamine (OAm) is employed as the solvent, the synthesis of Co particles from  $\text{Co(I)Cl(Ph}_3)_3$  ( $\text{Ph}=\text{C}_6\text{H}_5$ ) becomes complex due to the occurrence of two distinct time steps associated with equally distinct particle morphologies. Initially, spherical hcp cobalt nanoparticles grow within one hour at  $190^\circ\text{C}$ , followed by their dissolution and the subsequent recrystallization into rod-shaped nanoparticles over an extended period of ten hours. Only recently has a more profound understanding of the mechanisms underlying nanoparticle formation been achieved through a series of experimental and theoretical studies.<sup>6-8</sup> In the most

recent article titled *The five shades of oleylamine in a morphological transition of cobalt nanospheres to nanorods*,<sup>8</sup> some of the present authors reported on the intricate multifunctional role played by OAm, which is revealed to act as a disproportionation promoter, a surfactant, a source of H<sub>2</sub>, an oxidative etching promoter, and ultimately, a templating agent.

The current understanding of the reaction paths is the following. In the first stage, it is assumed that metallic cobalt and a Co(II) complex are formed according to a global disproportionation reaction:



where L is an unspecified ligand (PPh<sub>3</sub> or OAm). Indeed, Density functional theory (DFT) calculations<sup>6,7,9</sup> support the disproportionation hypothesis. OAm and triphenylphosphine being too “big”, the disproportionation reaction is modeled using the “smaller” NH<sub>3</sub> and PH<sub>3</sub> Lewis bases, respectively. When two reacting cobalt monomers are considered, calculations<sup>6,7</sup> point to the necessary phosphine/ammonia ligand exchange to avoid endothermic reactions. Subsequent theoretical calculations<sup>9</sup> by the same theory group examined disproportionation reaction paths starting from an already constituted cobalt dimer. Interestingly the reaction is not triggered by the displacement of the chloride, but by the asymmetric grouping of phosphine and ammonia molecules (e.g. all phosphine ligands on the same cobalt atom). This can lead to the electronic transfer of one electron from one cobalt to the other one (without change of the spin), and formation of a Co(0)(phosphine)-Co(II)(ammonia) pair. The nucleation and growth of metallic cobalt nanoparticles then begin.

The “cobalt sphere growth” is also accompanied by a noticeable release of H<sub>2</sub> (Figure 1) suggesting that OAm decomposes on the particle surfaces. H<sub>2</sub> is then in the capacity of reducing the Co(II) complex, the by-product of R1. In fact the Co(II) *plus* Co particle system is not stable. In a second stage, the freshly produced Co metal spheres are gradually “eaten up” and then

reappear in the form of elongated nanorods, whose electron diffraction pattern was interpreted as being due to a distorted form of hcp cobalt.<sup>6-8</sup> The micrographs in Figure 1 illustrate this spectacular transformation.

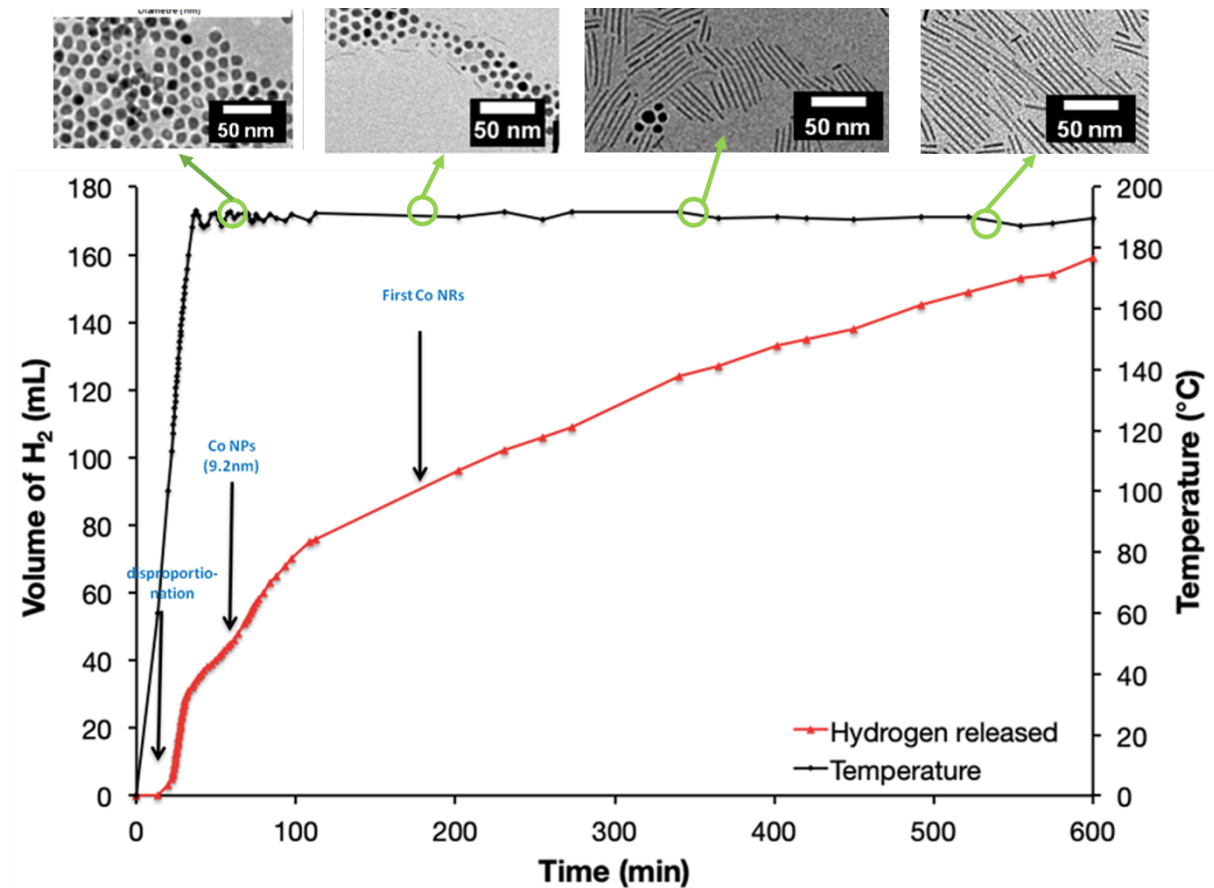
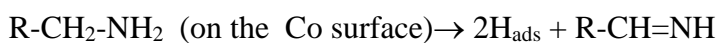


Figure 1. Temperature ramp and H<sub>2</sub> yield plotted against time. TEM investigation of the sphere to rod transition at various points of the synthesis time. The particle synthesis is made in pure OAm at 190°C under N<sub>2</sub>.

A mechanism explaining the sphere-to-rod transition mechanism is proposed in *Five shades of Oleylamine*.<sup>8</sup> To account for the H<sub>2</sub> yield (Figure 1), it is assumed that OAm adsorbs on the metallic Co spheres, breaks, to give adsorbed H atoms (H<sub>ads</sub>) and the aldimine:



R2

Then two  $H_{ads}$  recombine to give a  $H_2$  molecule that goes into the solution. As mentioned earlier,  $H_2$  reduces the  $Co(II)Cl_2L_2$  complex:



and cobalt nanorods start to grow in nanostructured areas of the TD:OAm solution.

R3 is followed by the acid-base reaction:



In turn, the cobalt spheres formed in the first stage are etched:



which produce new  $Co^{2+}$  ions that will be reduced by  $H_2$  via reaction R3. Then all metallic Co spheres are eventually consumed. *Co nanorods* and an ammonium-chloride salt result at the end of the process. The high aspect ratio of the produced particles is attributed to the templating role of OAm.<sup>8</sup>

Even though the model satisfactorily explains the observed growth phenomena, direct spectroscopic evidence of disproportionation was still lacking (i.e. determining the oxidation state of cobalt), as well as signatures of the amine decomposition products, namely aldimine (R2), and ammonium (R4). Therefore, after characterizing the precursor (in powder form), we employed X-ray Photoelectron Spectroscopy (XPS) to monitor nanoparticle growth kinetics by sampling the precursor solution at various times and temperatures. We used a 7:3 tetradecane:oleylamine mixture (denoted as 7:3 TD:OAm) to reduce the concentration of impurities in the solution (since OAm batches exhibit variability in composition), aiming to enhance the reproducibility of the reaction products. These were delicate experiments from an XPS perspective due to the dilution of the precursor. We further coupled this kinetic study with

characterization of films from centrifugated, washed nanoparticles, thus coated with a few layers of OAm.

The present study corroborated several aspects of the model delineated in *Five Shades of Oleylamine*,<sup>8</sup> including the occurrence of a disproportionation reaction during the sphere growth phase and the detection of ammonium. However, XPS spectroscopy also unveiled a more intricate chemistry of the system. Notably, it identified the existence of oxidized triphenylphosphine in the precursor Co(I) powder, co-existing with triphenylphosphine, although the role of the former is yet to be ascertained. Of significant interest, the XPS study brought to light an entirely unforeseen phenomenon: nanorods are in fact made of cobalt phosphide with a Co/P atomic ratio of  $\sim 0.5$ . This information prompted a complete reassessment of the crystallographic analyses conducted in our previous studies regarding the nanorods. While oleylamine deservedly plays the lead role in “*Five Shades*”, the organophosphorus ligands are equally important. This paper will therefore bring them to the spotlight.

## 2. Methods

### 2.1 Precursor synthesis

CoCl<sub>2</sub>·6H<sub>2</sub>O (Sigma-Aldrich, 98%), PPh<sub>3</sub> (fluorochem, 95%), NaBH<sub>4</sub> (Acros Organic, 95%) were commercially bought and used without further purification. Absolute ethanol and diethylether were degassed by bubbling argon gas for 15 minutes. OAm (70-98%) was bought from Sigma-Aldrich and degassed under argon bubbling.

Co(I)Cl(PPh<sub>3</sub>)<sub>3</sub> was prepared as follows. To 9.6 g of [CoCl<sub>2</sub>·6H<sub>2</sub>O], (40 mmol) and 32.0 g of triphenylphosphine (122 mmol) was added 600 ml of degassed ethanol. The resulting

heterogeneous solution was stirred vigorously at 60-70°C for 30 minutes environ to form in-situ the complex  $\text{Co(II)Cl}_2(\text{PPh}_3)_2$  as a bright blue powder. The mixture was then cooled down to 30°C, and 1.28 g of sodium borohydride was added (34 mmol) in 10 portions at a 10-minute interval. The color of the mixture changed from bright blue to dark brown. After 2 hours the brown precipitate was filtered under argon and washed sequentially with degassed ethanol, water, ethanol (until colorless solution was observed) and finally hexane (to dry it easily). The brown solid was dried under vacuum to give 25 g of the desired  $\text{Co(I)Cl(PPh}_3)_3$  complex with 75% yield (the other 25 % are mainly unreacted  $\text{CoCl}_2$  and triphenylphosphine together with some loss of the final complex stick in the glassware). This batch was added to the TD:OAm solution to produce the nanoparticles, and aliquots of this solution were examined with XPS (see below). Another batch was also washed several times with degassed diethylether to examine the effect of washing on the removal of residual free triphenylphosphine or its oxide using XPS.

## 2.2 Nanoparticle synthesis

In a glovebox under a nitrogen atmosphere, 0.25 mmol of  $\text{Co(I)Cl(PPh}_3)_3$  was added to a 10 mL mixture of TD and OAm. This mixture consisted of either 7 mL of TD and 3 mL of OAm or occasionally 9 mL of TD and 1 mL of OAm. The solution was placed in a 25 mL vial capped with a septum pierced by a pipette to provide overpressure. Stirring and heating were accomplished using a 50 mL "drysyn" filled with sand. The temperature was gradually increased from 20 to 190°C over the course of 1 hour to produce cobalt nanospheres. Aliquots were periodically withdrawn from the solution at various times and temperatures to facilitate a pseudo-kinetic study using XPS analysis during the nanosphere growth stage. For the production of nanorods, the solution was maintained at 190°C for an additional 9 hours.

To prepare films of concentrated nanoparticles suitable for analysis by XPS or TEM, the solution was cooled to room temperature, and the nanoparticles were washed by adding 20 mL of ethanol and centrifuging for 5 minutes at 2500 rpm. The resulting solid was then dispersed in toluene.

### **2.3 Transmission Electron Microscopy Measurements**

Sample Characterization. Transmission Electron Microscopy (TEM). A 100 kV (TEM, JEOL JEM-1011 with a digital camera Gatan) was used to characterize cobalt nanocrystals and their assemblies (low magnification bright field picture, Selected Area Electron Diffraction, SAED). To observe the nanoparticles, 10  $\mu\text{L}$  of the solution containing dispersed nanoparticles in toluene were deposited on a TEM grid, followed by evaporation of the solvent in order to form a nanoparticle film.

### **2.4 X-ray photoelectron spectroscopy (XPS)**

#### *2.4.1 Set-up*

The XPS setup installed at “Laboratoire de Chimie Physique, Matière et Rayonnement” (UMR CNRS 7614), is part of the XPS platform of the “Institut Parisien de Chimie Physique et Théorique” (FR CNRS 2622) of Sorbonne University. The Al  $K_{\alpha}$  monochromatized source (SPECS FOCUS 500,  $h\nu=1486.71$  eV) is operated at 10 kV, with an anode current of 25 mA (250 W). The electron analyzer is a SPECS PHOIBOS 150, fitted with a delay line detector. Measurements are made at normal electron takeoff. The X-ray spot has a dimension  $0.5\text{mm}\times 3.5$  mm. The Medium Area Mode is used. The spectrometer resolution is defined by the pass energy of 20 V and the entrance slit width of 7 mm. To determine the overall resolution (photons and

spectrometer), the Fermi edge of a clean Co foil is measured. Its derivative is a Gaussian with a FWHM of 495 meV. As measurements are made at  $T=300\text{ K}$  ( $k_{\text{B}}T=25\text{ meV}$ ), this value can be considered as a good estimation of the overall experimental resolution. The inflection point of the Fermi edge gives the Fermi level of the analyzer.

Samples examined in the UHV analysis chamber were powders ( $\text{Co(I)Cl(PPh}_3)_3$ ,  $\text{Co(II)Cl}_2(\text{PPh}_3)_2$  and pure  $\text{PPh}_3$ ), aliquots of the reaction mixture and washed, centrifugated nanoparticle films. Powders were pressed on a conductive carbon tape. To study the kinetics of the Co nanoparticle synthesis, aliquots were taken from the reaction “pot” containing the  $\text{Co(I)Cl(PPh}_3)_3$  precursor dissolved in a 7:3 TD:OAm solution. Typically, three droplets of 10  $\mu\text{L}$  each were deposited on a ( $n^+$  doped) conductive silicon wafer. To minimize the interaction with air, the solution samplings were prepared in a glove box and kept under vacuum in a sealed sample container (pressure  $10^{-2}$  mbar) for less than one hour. Then they were introduced in the XPS load-lock chamber (base pressure  $10^{-6}$  mbar) and let to degas for 12-18 hours until the pressure drops down to  $10^{-6}$  mbar. Concentrated particle films were also deposited as solution droplets on the silicon wafer, and the toluene solvent was let to evaporate in the load-lock.

After introduction into the UHV analysis chamber, the films were studied by XPS under a pressure in the  $10^{-10}$  mbar range. To obtain sufficient statistics, the total measurement duration was typically 12 hours.

#### *2.4.2 Charging and flood gun operation*

The substrates supporting powders and films, the metallic sample holder and the electron analyzer are all conductive, electrically connected and grounded. This means that their common BE reference is the Fermi level. However, powders, solution films, and washed nanoparticle films we are dealing with are all insulating. This means that charging is observed upon X-ray beam irradiation (photoelectrons and Auger-electrons are emitted out of the sample and the

resulting positive charge is not compensated by electrons from the ground). The reference to the analyzer Fermi level is lost.<sup>10</sup> Charging leads to a displacement of the XPS peaks to higher BE, or even to peak disappearance for the peaks with the smallest KE (e.g. Co 2p in our case).

We used a flood gun to enable the XPS measurement. We kept the sample holder grounded to avoid discharging times commensurate with a spectrum acquisition in the swept mode.

Differential charging effects must be carefully monitored, as it distorts the peaks. The effect of the flood gun in controlling the equipotentiality of the insulator surface can be better appreciated considering the symmetry of the “single-component” core-levels (C 1s, N 1s) and the value of their full-width-at-half-maximum (FWHM) is minimized.

As the analyzer Fermi level reference is lost, the BE of C 1s is taken at 285 eV. This choice is commonly adopted as a reasonable value for alkane chains.<sup>11</sup> Indeed in organic systems supposed to be in thermodynamic equilibrium with a metal substrate (the film is sufficiently thin to allow electron exchange), such as self-assembled monolayers on gold, C 1s is found at 284.8 eV for dodecanethiol<sup>12</sup> and 285.0 eV for tridecanethiol.<sup>13</sup> Therefore, C 1s at 285 eV is a valid choice for OAm and the TD:OAm mixtures. For the phenyl moiety in triphenylphosphine, we adopt the same C 1s reference energy, following a previous publication.<sup>14</sup>

#### *2.4.3 Argon sputtering*

Films of concentrated nanoparticles were also submitted to Ar sputtering to diminish the organic capping layer, under the following conditions: Ar pressure of  $10^{-5}$  mbar, ion energy of 1 keV, emission current of 3 mA, sample current of 5  $\mu$ A, and etching time equal to 5 min.

#### 2.4.4 Element quantification

The procedure leading to element quantification is defined in detail in the SI, section S1. It starts from the measurement of the XPS intensities  $I_{X\ CL}$  (see Tables S1 and S2 of the SI) and considers the following parameters: the atomic core-ionization cross-section of a given core-level (CL) of atom X  $\sigma_{X\ CL}$ ,<sup>15</sup> the photoelectron *mean free path*  $\lambda_{X\ CL}$  (Figure S1 of the SI), and the lens/analyzer transmission  $T_{lens}$ .  $\sigma_{X\ CL}$  depends on  $h\nu$  (fixed at 1486.71 eV) and both  $\lambda_{X\ CL}$  and  $T_{lens}$  depend on the photoelectron kinetic energy (KE). We define in section S1 of the SI a sensitivity factor  $Q_{X\ CL} = f(\sigma_{X\ CL}, \lambda_{X\ CL}, T_{lens})$ . Calculated  $Q_{X\ CL}$  values are given in Table S3 of the SI. Then we obtain the normalized atom X core-level (CL) intensity  $I_{X\ CL}^{norm}$  by dividing  $I_{X\ CL}$  by  $Q_{X\ CL}$ :

$$I_{X\ CL}^{norm} = \frac{I_{X\ CL}}{Q_{X\ CL}} \quad \text{Equation 1}$$

Useful  $\frac{I_{X\ CL}^{norm}}{I_{Y\ CL}^{norm}}$  ratios are collected in Table S4 of the SI. Only for samples that are homogeneous

in-depth, does  $\frac{I_{X\ CL}^{norm}}{I_{Y\ CL}^{norm}}$  correspond to the “atomic ratios”  $\frac{[X]}{[Y]}$  of elements X and Y. Since the ratio

$\frac{I_{Co\ 3p}^{norm}}{I_{Co\ 2p}^{norm}}$  is 1 for a homogeneous sample (e.g. the cleaned Co foil), any departure from 1, see Figure

S2, is indicative of cobalt atoms that are not evenly distributed in the depth of the material.

Indeed, the XPS probing depth is sizably different for Co 3p (KE~1436 eV) and Co 2p (KE~706

eV) photoelectrons because of their inelastic mean free path  $\lambda$  ratio  $\frac{\lambda_{Co\ 3p}^{medium}}{\lambda_{Co\ 2p}^{medium}}$  of ~1.7.

### 3. Results and discussion

#### 3.1 The Co(I) and Co(II) complexes powders

Co(II)Cl<sub>2</sub>(PPh<sub>3</sub>)<sub>2</sub> and Co(I)Cl(PPh<sub>3</sub>)<sub>3</sub> powders were characterized by XPS. The blue Co(II)Cl<sub>2</sub>(PPh<sub>3</sub>)<sub>2</sub> powder is the starting product for the synthesis of Co(I)Cl(PPh<sub>3</sub>)<sub>3</sub>. Additionally, it provides a Co(II) spectroscopic standard.<sup>7</sup>

$\frac{I_{Co\ 3p}^{norm}}{I_{Co\ 2p}^{norm}}$  is 1.04 for the Co(II) powder, 1.07 for the Co(I) powder batch resulting directly from the synthesis (no washing in diethylether), and 0.95 after washing of the latter in diethylether, as shown in Figure S2 of the SI. A deviation of less than 10% is indicative that cobalt atoms are homogeneously distributed in the depth of the samples.

The Co 2p spectra of the Co(II) complex and of the Co(I) precursor (no-diethylether washed powder, and diethylether-washed powder) are shown in Figure 2. As the Co 2p spectrum is actually a doublet with the 2p<sub>1/2</sub> and 2p<sub>3/2</sub> components separated by ~15 eV, the large spin-orbit splitting enables us to limit our discussion to the 2p<sub>3/2</sub> component. In both cases, the Co 2p<sub>3/2</sub> spectrum consists in a main peak (m) at ~781 eV, followed by a broad satellite (sat) at higher binding energy (BE), ~786 eV. Diethylether washing has no effect on the Co(I) spectral shape. In addition, the Co 2p spectra of the Co(II) and Co(I) complexes are very similar, despite the different oxidation states of the metal. In fact, the similarity may result from their non-zero spin. Co(II)Cl<sub>2</sub>(PPh<sub>3</sub>)<sub>2</sub> is a paramagnetic tetrahedral complex, with S equal to 3/2. The Co(I)Cl(PPh<sub>3</sub>)<sub>3</sub> complex is also tetrahedral with S equal to 1.<sup>16,7,9</sup> In contrast, we show in the SI, Figure S3, that the Co 2p spectra of the low spin (S=0) complexes HCo(I)(P(OPh)<sub>3</sub>)<sub>4</sub> and HCo(I)(PhP(OEt)<sub>2</sub>)<sub>4</sub>, that adopt a trigonal bipyramidal symmetry, present an extremely weak satellite and a considerably narrower main peak. Generally speaking, the main peak and satellite shape of transition metal 2p core level is highly dependent on the (symmetry and ligand related) molecular orbital scheme *in the core-ionized state* (see the paradigmatic case of Cu<sup>2+</sup> in ref<sup>17</sup>).

The Cl 2p core-level, see Figure 3(a), is actually a doublet with two components  $2p_{1/2}$  and  $2p_{3/2}$  separated by a spin-orbit splitting of 1.6 eV. Fitting curves with BE position and full-width at half maximum (FWHM) are also plotted. The BE of Cl  $2p_{3/2}$  is found at 198.4 eV in  $\text{Co(II)Cl}_2(\text{PPh}_3)_2$  (Blackburn et al.<sup>14</sup> found  $198.9 \pm 0.5$  eV for  $\text{Cl}^-$  coordinated to +II metals in  $\text{M(II)Cl}_2(\text{PPh}_3)_2$  (M=Ni, Cd, Pd)). Cl  $2p_{3/2}$  is also found at 198.4 eV in the Co(I) complex. Therefore the Cl 2p BEs of the chloride ion in the Co(I) and Co(II) complexes are not sensitive to the metal ion charge.

Figure 3(a) illustrates the P 2s spectrum of the Co(II) complex, which exhibits a single component at 189.3 eV. Similarly, the pure  $\text{PPh}_3$  powder displays a *single component* at 188.8 eV. In contrast, the P 2s spectrum of the Co(I) powder reveals *two components* separated by approximately 2 eV: one at 190.5 eV and the other at 188.4 eV. This suggests the presence of phosphorus in two distinct chemical environments, with the low binding energy (BE) component attributable to  $\text{PPh}_3$  (see the discussion of the P 2p spectrum below). Notably, washing the sample in diethylether increases the intensity of the low BE component.

The P 2p core-level spectrum is also a spin-orbit split doublet, with a BE difference of 0.8 eV between the  $2p_{1/2}$  and  $2p_{3/2}$  peaks. The P 2p spectrum of the Co(II) complex shown in Figure 3(b) can be fitted with *a single doublet*, featuring a P  $2p_{3/2}$  BE of  $\sim 131.5$  eV. This value is consistent with the BE observed in  $\text{M(II)Cl}_2(\text{PPh}_3)_2$  complexes (M = Ni, Cd, Pd).<sup>14</sup> Furthermore, the P  $2p_{3/2}$  BE is close to that of the uncoordinated ligand, which is 131.2 eV (the average P  $2p_{3/2}$  BE of  $\text{PPh}_3$  is  $131.0 \pm 0.4$  eV considering 18 literature values in the NIST<sup>18</sup> database). In contrast, the P 2p spectrum of the Co(I) complex is fitted by *two doublets*, confirming the P 2s spectra fitting with two components. Washing the sample in diethylether leads to an increase in the intensity of the low BE doublet, also consistent with the changes observed in the P 2s spectra. The lower BE component ( $2p_{3/2}$  at  $\sim 130.8$  eV) is attributed to  $\text{PPh}_3$ , whereas the higher BE component ( $2p_{3/2}$  at  $\sim 132.8$  eV) corresponds to *an oxidized form of PPh<sub>3</sub>*.

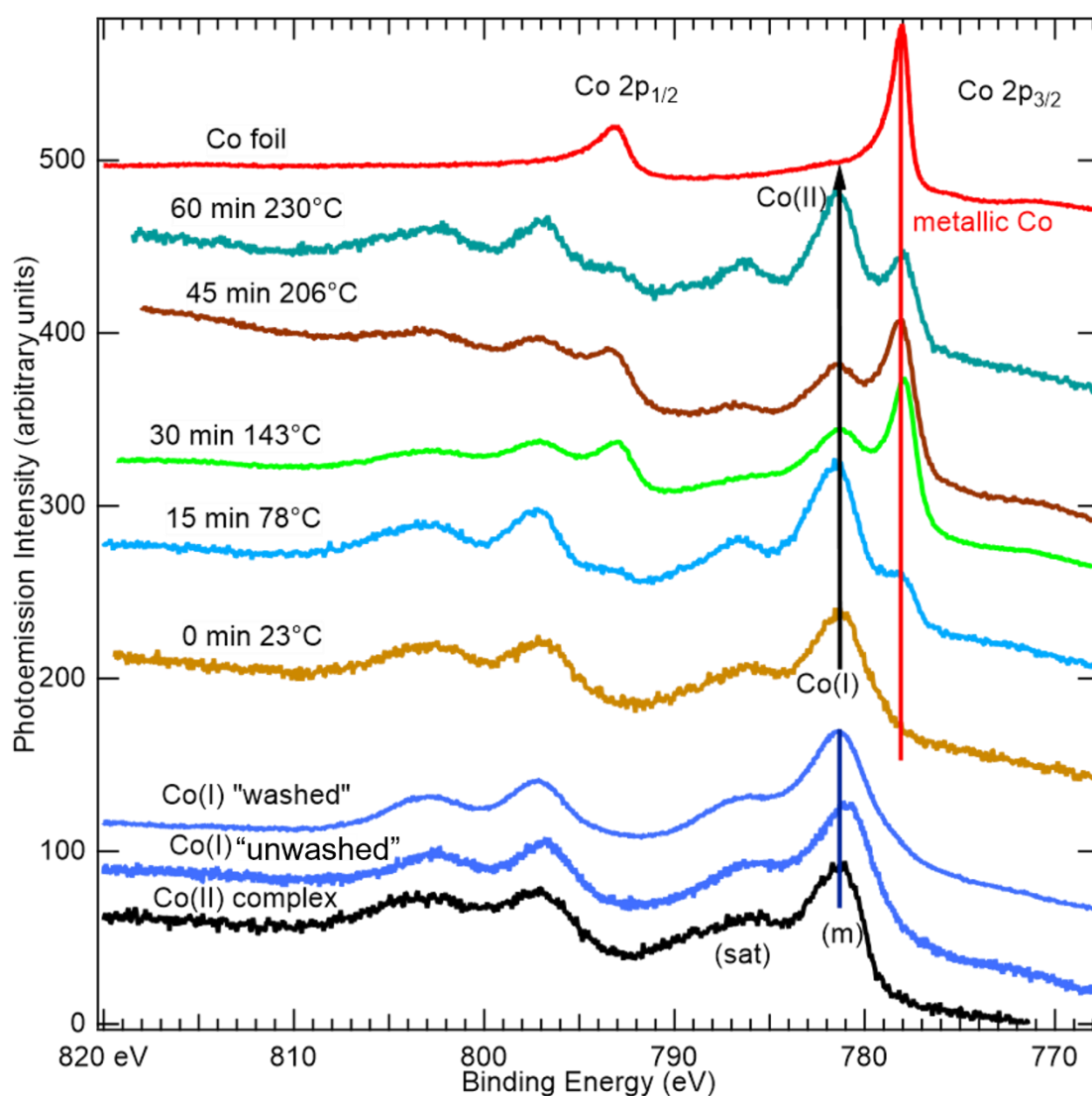
Triphenylphosphine oxide (O=PPh<sub>3</sub>) has a P 2p BE of 132.9 eV.<sup>14</sup> For its part, the P 2p<sub>3/2</sub> BE of the P(OPh)<sub>3</sub> phosphite ligand, which coordinates the zero spin HCo(I)(P(OPh)<sub>3</sub>)<sub>4</sub> complex, is 133.3 eV (Figure S3 of the SI). However, the BE of the phosphonite ligand in HCo(I)(PhP(OEt)<sub>2</sub>)<sub>4</sub>, which is 132 eV (Figure S3), is too small to be responsible for the red-shaded component in Figure 3(b).

PPh<sub>3</sub> can be oxidized by O<sub>2</sub> molecules during the exposure of the Co(I) complex to air before XPS measurements. Similar to the mechanism of M(0)(PPh<sub>3</sub>)<sub>4</sub>-catalyzed oxidation of PPh<sub>3</sub> (M=Pt or Pd),<sup>19,20</sup> Co(I)Cl(PPh<sub>3</sub>)<sub>3</sub> could capture an O<sub>2</sub> molecule to form a peroxophosphine complex Co(III)Cl(PPh<sub>3</sub>)O<sub>2</sub>, increasing the formal oxidation state of Co from +I to +III. Then this intermediate peroxophosphine complex would rearrange to provide the oxidized ligand. While the oxidation of PPh<sub>3</sub> atom to O=PPh<sub>3</sub> is reported in the literature,<sup>19,20</sup> the formation of the phosphite P(OPh)<sub>3</sub> is not. Indeed, on thermodynamic considerations only the formation of triphenylphosphine oxide should be preferred to the insertion of one O atom in the P-C bond, at least in the gas phase. Gas phase calculations show indeed that the ΔG of the reaction PPh<sub>3</sub> + ½O<sub>2</sub> → O=PPh<sub>3</sub> is -77 kcal.mol<sup>-1</sup>, while it is only -57 kcal.mol<sup>-1</sup> for the reaction PPh<sub>3</sub> + ½O<sub>2</sub> → P(OPh)Ph<sub>2</sub>.<sup>21</sup>

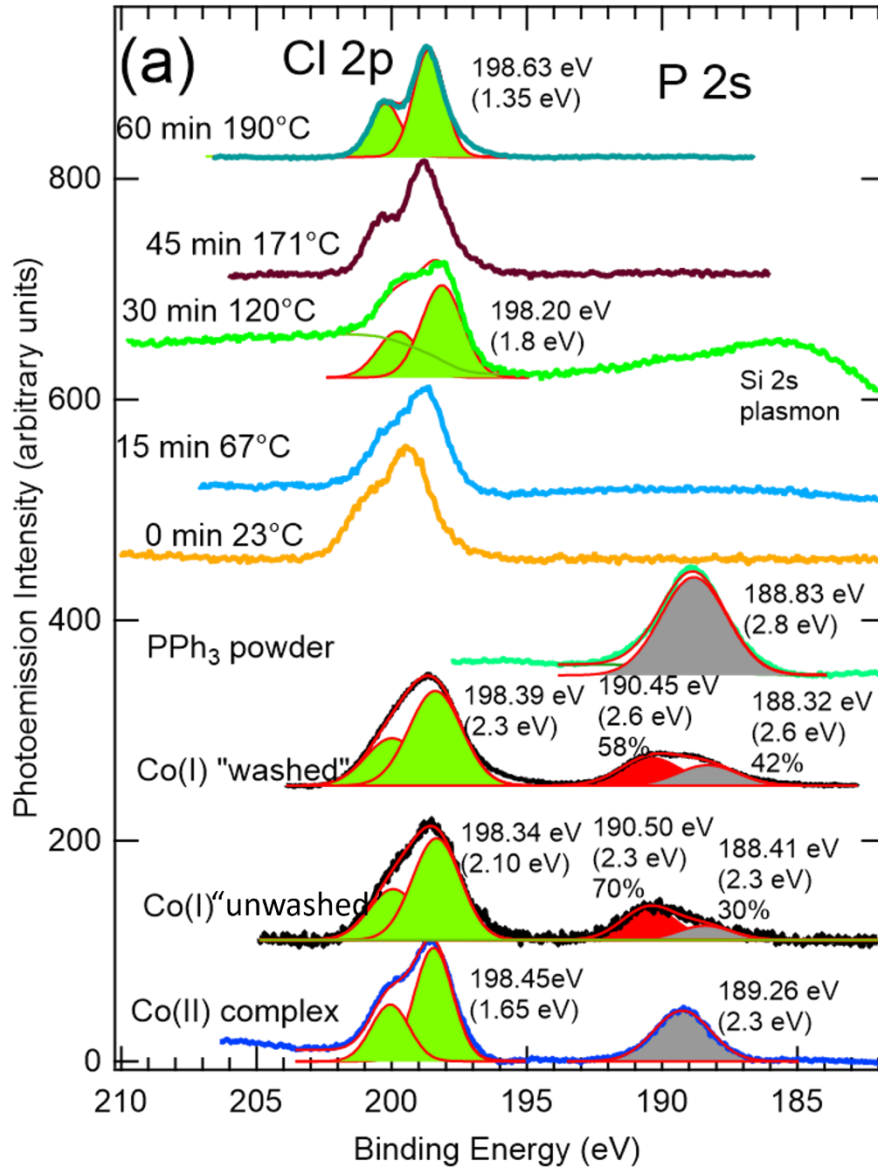
It is worth noting that both the PPh<sub>3</sub> powder itself and the PPh<sub>3</sub> ligands of the Co(II) complex remain unoxidized (Figure 3(b)), even when transferred to the UHV chamber under the same conditions as the Co(I) complex. In fact, the oxidation of the PPh<sub>3</sub> ligand by O<sub>2</sub> is unique to the Co(I) complex, because the reaction scheme implying a peroxophosphine intermediate is impossible for Co(II)Cl<sub>2</sub>(PPh<sub>3</sub>)<sub>2</sub>. The Co(IV)Cl<sub>2</sub>(PPh<sub>3</sub>)<sub>2</sub>O<sub>2</sub> intermediate cannot be formed, Co(III) being the maximum “common” oxidation state of cobalt.

In contrast to the XPS analysis, a <sup>31</sup>P Nuclear Magnetic Resonance (NMR) of Co(I)Cl(PPh<sub>3</sub>)<sub>3</sub> dissolved in OAm (SI of ref <sup>7</sup>) in which PPh<sub>3</sub> is displaced by the amine shows that the latter

ligand remains unoxidized. The expected P/Co stoichiometric ratio of 3 is also found. This discrepancy with the XPS information likely arises from the latter technique's surface sensitivity. In fact, phosphine oxidation may be limited to the surface of the powder grains. Nonetheless the presence of an oxidized  $\text{PPh}_3$  species, even at low concentration in the powder, should be considered in the discussion of the reaction mechanisms. In the same vein, quantitative XPS analysis (section S1.3 of the SI) suggests that the Co(I) powder is deficient in phosphorus, which is not the case of the Co(II) powder.



*Figure 2.* Co 2p spectra of the  $\text{Co(II)Cl}_2(\text{Ph}_3)_2$  and  $\text{Co(I)Cl}(\text{Ph}_3)_3$  complexes (powders), and of aliquots of the (7:3) TD:OAm solution taken at 0 min ( $23^\circ\text{C}$ ), 15 min ( $67^\circ\text{C}$ ), 30 min ( $120^\circ\text{C}$ ), 45 min ( $171^\circ\text{C}$ ), and 60 min ( $190^\circ\text{C}$ ), respectively. The cobalt concentration in the mixture is  $2.5 \cdot 10^{-2} \text{ mol}\cdot\text{L}^{-1}$ . The Co 2p spectrum of the clean Co foil is also given as a standard of metallic Co. All BE are referenced to the C 1s peak positioned at 285.0 eV, except for the Co foil spectrum, referenced to the Fermi level. Note that “unwashed” refers to the as-produced Co(I) complex powder (without diethylether washing), while “washed” denotes the Co(I) complex powder washed several times in diethylether.



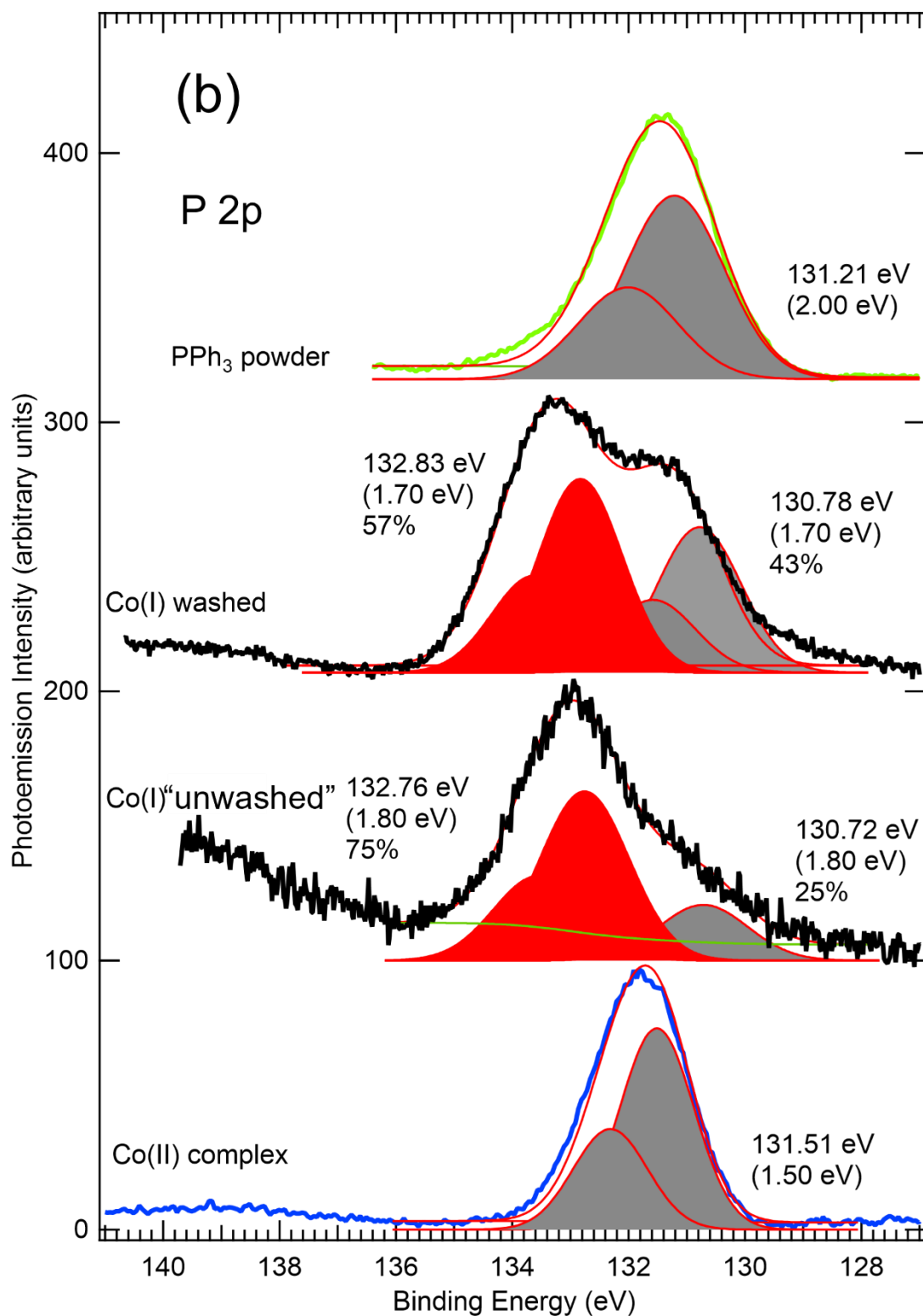


Figure 3. (a) Cl 2p and P 2s core-levels of the Co(II) and Co(I) complexes (powders), of the PPh<sub>3</sub> powder and of aliquots of the 7:3 TD:OAm solution (precursor concentration =  $2.5 \times 10^{-2}$  mol.L<sup>-1</sup>) taken at 0 min (23°C), 15 min (78°C), 30 min (143°C), 45 min (206°C), and 60 min

(230°C), respectively. (b) P 2p core-levels of the Co(II) and Co(I) complexes and of the PPh<sub>3</sub> powder. All BE are referenced to the C 1s peak positioned at 285 eV. A monochromatized Al K<sub>α</sub> source (1486.71 eV) was used. The experimental curves are fitted with sums of Gaussians (red solid curves), whose BE positions of Cl 2p<sub>3/2</sub>, P 2s and P 2p<sub>3/2</sub> components, FWHMs (between parentheses) and spectral weights (%) are also given. Note that “unwashed” refers to the as-produced Co(I) complex powder (without diethylether washing), while “washed” denotes the Co(I) complex powder washed several times in diethylether.

### 3.2 Kinetic study of Co particle synthesis

The nominal Co(I)Cl(PPh<sub>3</sub>)<sub>3</sub> precursor was dissolved into the 7:3 TD:OAm solution and submitted to the temperature ramp shown in Figure 1. We used the Co(I) precursor batch, *with no further washing in diethylether* (see **METHODS**). Aliquots taken at various steps of the synthesis from the TD:OAm “pot” were deposited on a conductive silicon substrate. The precursor concentration in the reaction mixture is  $2.5 \times 10^{-2} \text{ mol}\times\text{L}^{-1}$ . This corresponds to a number of cobalt atoms per unit volume, denoted as  $n_{\text{Co}}^{\text{TD:OLAm}}$ , of  $1.5 \times 10^{19} \text{ Co atoms}\times\text{cm}^{-3}$ , to be compared with the atomic concentration in metallic cobalt  $n_{\text{Co}}^{\text{metal}}$ , which is  $9 \times 10^{22} \text{ Co atoms}\times\text{cm}^{-3}$ . XPS is commonly employed to characterize solid surfaces. However, transitioning to solutions with a low concentration of solutes presents a significant challenge. Here, the cobalt atom concentration  $n_{\text{Co}}^{\text{TD:OLAm}}$  is nearly four orders of magnitude smaller than  $n_{\text{Co}}^{\text{metal}}$ . The success of this approach relies on efficient detection, which is facilitated by the low noise delay-line detector of our current setup. To the best of our knowledge, this study represents the first instance of a *pseudo in situ* kinetic investigation of metal particle synthesis monitored by XPS.

The deposited films presented a smooth aspect in the XPS chamber. Most films were continuous and sufficiently thick to completely mask the contribution of the Si core-levels of

the substrate. As more than 95% of the photoelectrons are inelastically scattered when the photoelectron is emitted in TD:OAm at a depth more than three times the photoelectron inelastic mean free paths  $\lambda$  (values are given in Figure S1), aliquot film thicknesses are significantly greater than 11 nm. Occasionally the Si 2s plasmons appeared in the P 2s BE range, see e.g. Figure 3(a), due to film discontinuities. As for powders, charging phenomena were observed, and the flood gun was operated. After centrifugation and washing the solid part of aliquots was studied by TEM to provide the size distribution of the particle shown in Figure 4.

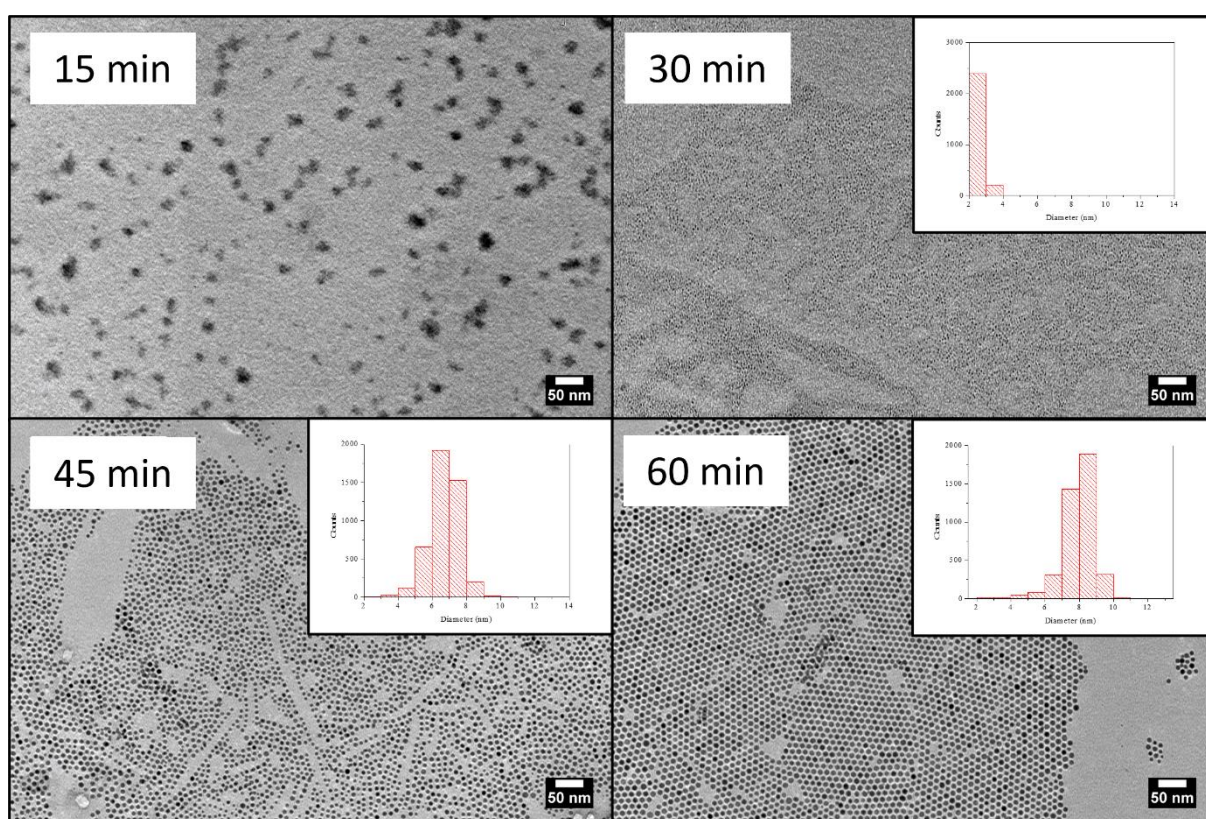


Figure 4. TEM micrographs and particle size distribution of the solid part obtained after centrifugation of the aliquots. Co particles are not detected in the “0 min–23°C” and the “15 min”–67°C centrifugated aliquots. The sphere diameters are  $2.3 \pm 0.4$  nm (120°C–30 min),  $6.7 \pm 0.9$  nm (171°C–45 min), and  $7.9 \pm 1.0$  nm (190°C–60 min).

The N 1s spectra and the calculated  $\frac{I_{C\ 1s}^{norm}}{I_{N\ 1s}^{norm}}$  ratios are shown in Figure S4 and Figure S5 of the SI, respectively. Under UHV conditions, 99% pure OAm becomes solid. The  $\frac{I_{C\ 1s}^{norm}}{I_{N\ 1s}^{norm}}$  ratio is  $\sim 38$ , far greater than the expected C/N stoichiometric ratio of 18. This means that the OAm molecules are preferentially oriented in the pure molecular film. This can be explained considering that the long carbon tail is directed outward from the surface in pure OAm films, damping the N 1s photoelectrons yield. For the 7:3 TD:OAm mixtures, we do not find stoichiometric ratios either. Figure S5 shows that  $\frac{I_{C\ 1s}^{norm}}{I_{N\ 1s}^{norm}}$  is 28 for the “0 min 23°C” sample, and  $\sim 24 \pm 2$  for the aliquots taken in the 78°C to 230°C range. These values are significantly lower than the atomic C/N ratio equal to 59 for the 7:3 mixture. The nitrogen enrichment in the surface layers suggests that the aliquots solidified under UHV are vertically structured.

For all aliquots, the normalized XPS intensity ratio,  $\frac{I_{Co\ 3p}^{norm}}{I_{Co\ 2p}^{norm}}$  is given in Figure S2 of the SI.  $\frac{I_{Co\ 3p}^{norm}}{I_{Co\ 2p}^{norm}}$  depends both on the particle size and on its in-depth distribution in the TD:OAm solvent. When the particle size is 8 nm (60 min- 190°C),  $\frac{I_{Co\ 3p}^{norm}}{I_{Co\ 2p}^{norm}}$  reaches  $\sim 1.8$ . This value is typical of a cobalt particle covered by one monolayer of OAm (see below).

We start discussing the XPS spectra of the “0 min–23°C aliquot”. The shape of the Co 2p spectrum and the Co 2p<sub>3/2</sub> BE position, at 781.4 eV, are not much affected (Figure 2) with respect to those of the Co(I) complex powder. There is no solvent effect. The broad main peak and the strong satellite show that Co(I) remains *high-spin* when the precursor is diluted in TD:OAm. The other important information contained in the Co 2p spectrum is that the formation of metallic cobalt is not observed at a Co 2p<sub>3/2</sub> BE of 778.1 eV (the Co 2p<sub>3/2</sub> BE of the cleaned Co foil, referenced to the Fermi level of the analyzer, see Figure 2). The fact that the disproportionation of the Co(I) complex does not occur in OAm at room temperature stands

in stark contrast to the case when this precursor is dissolved in tetrahydrofuran (THF). In this solvent, *pure* cobalt nanoparticles of approximately 10 nm in size are readily formed at 23°C, see the SI, section S5 for more details.

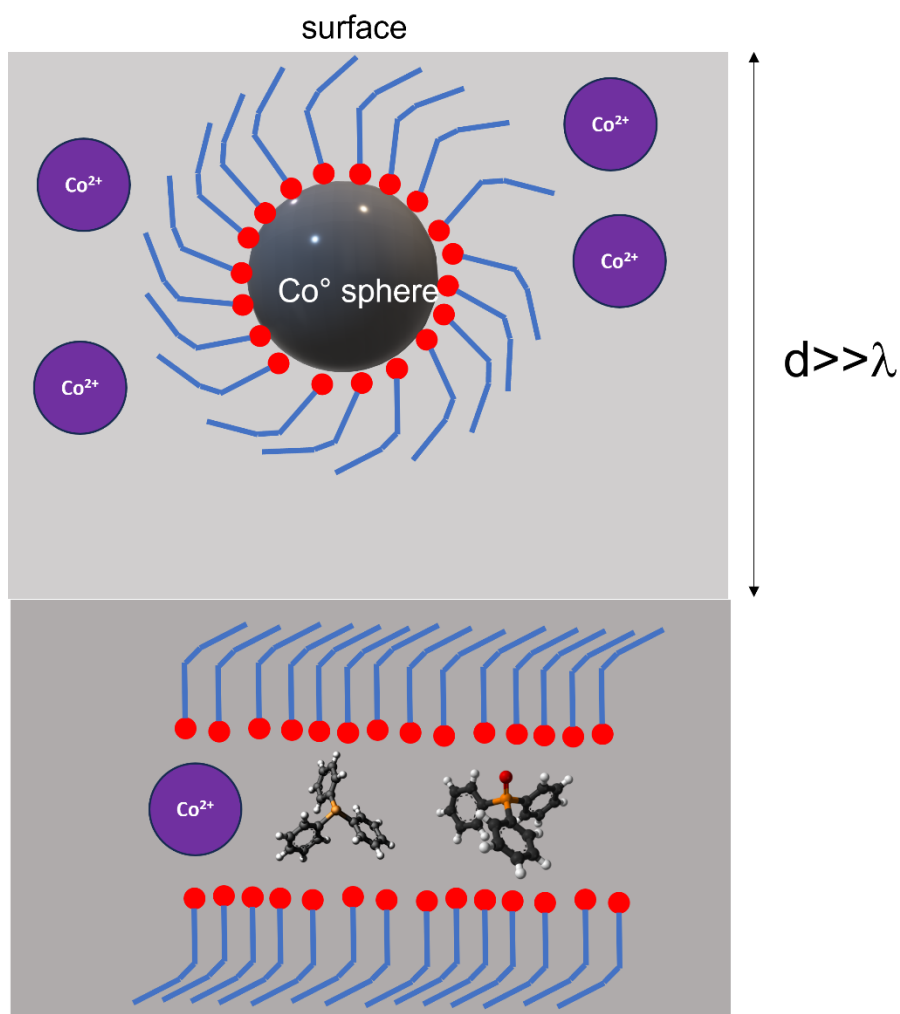
Solvation of the precursor in the TD:OAm mixture does not affect the BE of the Cl 2p<sub>3/2</sub> peak (Figure 3(a)) either, as it remains aligned with that of the Co(I) precursor, showing that chlorine remains Cl<sup>-</sup>. However, once the precursor is in solution (Figure 3(a)), the P 2s signal disappears from the XPS probed layers ( $\frac{I_{P\ 2s}^{norm}}{I_{Co\ 3p}^{norm}} = 0$ ), while the cobalt and chlorine XPS signals remain well visible ( $\frac{I_{Cl\ 2p}^{norm}}{I_{Co\ 3p}^{norm}} = 2.8$ ). Naturally the P 2p core-level is also non-measurable. In fact, we know that phosphorus has not left the solution, as we find it again in the concentrated nanoparticle films obtained after centrifugation and washing (see next subsection). These observations have profound consequences we detail below.

First, this means that OAm *fully substitutes* the organophosphorus ligands around the Co<sup>+</sup> ion once the precursor is solvated. After the XPS analysis of the precursor powders, questions can legitimately be asked about the nature the organophosphorus ligands in the precursor powder, about their number around the metal, all of which having a potential impact on the electronic structure of the cobalt ion. Such concerns fade out when OAm becomes the exclusive ligand in the reaction mixture. One can consider that the Co 2p spectrum of Co<sup>+</sup> in TD:OAm is the *standard* of high spin Co(I). Note it is identical to that of the powder, specifically the original batch that was not washed in diethylether, as well as the diethylether-washed powder.

Second, we must consider that the solidified solution is “vertically” structured (with an OAm propensity for the surface). SAXS measurements indicate that pure OAm is indeed periodically structured.<sup>8</sup> This would create natural “sinks” well below the surface where the organophosphorus ligands accumulate (see Scheme 1). The depth at which they concentrate

must be significantly larger than  $\sim 3\lambda$ , that is  $\sim 11$  nm (the P 2s and P 2p electrons in TD:OAm are respectively  $\sim 3.5$  and  $\sim 3.7$  nm, see Figure S1).

When the synthesis temperature is raised above  $23^\circ\text{C}$ , sizeable changes are observed in the Co 2p spectra. The Co  $2p_{3/2}$  spectrum of the “15 min– $67^\circ\text{C}$ ” sampling (Figure 2) now exhibits a shoulder at  $\sim 778$  eV distinctively shifted from the main peak position at 781.3 eV. *This component is characteristic of metallic cobalt.* However, the TEM micrograph in Figure 4 does not yet show any presence of nanoparticles at this stage, probably because they are too small to be imaged. This emphasizes the complementarity between XPS spectroscopy and TEM. The Cl 2p spectrum of the “15 min– $67^\circ\text{C}$ ” sampling (Figure 3(a)) is broader than that of the “0 min– $23^\circ\text{C}$ ” sampling (this is likely an effect of differential charging that is not well compensated), but the Cl  $2p_{3/2}$  BE is at 198.7 eV, which shows that there is no change in the oxidation state of chlorine ( $\text{Cl}^-$ ). *The P 2s (Figure 3 (a)) and P 2p signals continue to be unobservable when synthesis time and temperature both increase.*



Scheme 1. Scheme explaining the disappearance of the phosphorus XPS signal. The organophosphorous ligand ( $\text{PPh}_3$  and/or one of its oxidized form, e.g.  $\text{OPPh}_3$ ) accumulates in sinks well below the surface at a distance  $d$  significantly greater than the P 2s/P 2p photoelectron inelastic mean free paths  $\lambda$  (3.5-3.7 nm). OAm is represented by a red round head ( $\text{NH}_2$ ) and a blue tail (carbon chain). Chloride ions are not represented.

For the “30 min–120°C”, “45 min–170°C” and “60 min–190°C” aliquots, the Co nanoparticles can now be imaged, see Figure 4, having reached diameters of  $2.3 \pm 0.4$  nm,  $6.7 \pm 0.9$  nm and  $7.9 \pm 1.0$  nm, respectively. Then the metallic peak at  $\sim 778$  eV is well marked. In the context of a disproportionation reaction,<sup>7</sup> the Co  $2p_{3/2}$  peak at  $\sim 781.3$  eV should be now

attributed to the  $\text{Co}^{2+}$  ion in the Co(II) complex, as the Co 2p spectra of Co(II) and high spin Co(I) complexes cannot be distinguished (see the powder spectra). Note that the photoemission intensity ratio between metallic cobalt and Co(II) is smaller for the “60 min” sampling than for the “30 min” and “45 min” ones. It is possible that bigger particles are on average more below the film surface than smaller ones.

The Cl  $2p_{3/2}$  BE found in the  $198.4 \pm 0.2$  eV range shows that chlorine remains in the form of a chloride ion. The average N 1s BE of  $399.6 \pm 0.6$  eV (five measurements, see Figure S4 of the SI) is comparable to the average BE of amines (a value of  $399.0 \pm 0.3$  eV is calculated considering a total of 6 R-NH<sub>2</sub> BE extracted from the NIST database<sup>18</sup>). Given the low concentration of the precursor ( $2.5 \times 10^{-2}$  mol.L<sup>-1</sup>), it is expected that OAm molecules affected by a reaction at the Co particle surface (leading to ammonium and aldimine species) will not be detectable.

To summarize, the study by aliquots clearly demonstrates the disproportionation of Co(I) into metallic cobalt and cobalt II, within the temporal range of 0 min – 60 min and thermal range of 23°C – 190°C. Another important finding is the complete disappearance of the phosphorus signal in the film depth probed by XPS, which implies that the spherical particles created in the 7:3 mixture are made of pure cobalt. Indeed, there is no sign of surface phosphidation of these spherical particles. This finding aligns perfectly with all the structural characterizations (HR-TEM, SAED, or XRD) conducted on Co spheres under the form of concentrated films, which consistently reveal pure metallic Co with an hcp crystalline structure (refer to refs <sup>6-8</sup>). In deeper layers inaccessible to XPS (see scheme 1), where organophosphorus ligands have retreated, it is however possible that metallic phosphide particles have already formed. Their size may be very small, as they were not detected by microscopy in concentrated, centrifugated samples.

### 3.3 Concentrated nanoparticle films

Concentrated nanoparticles films of *spheres*, *spheres-and-rods*, and *rods* whose TEM micrographs are shown in Figure 5 were prepared from centrifugated TD:OAm solutions washed in ethanol and dispersed in toluene. Particles are prepared in the 7:3 TD:OAm mixture (as for the kinetic study), but a synthesis of spheres in the 9:1 TD:OAm mixture was also examined. The 9:1 mixture is considered by the authors of *Five Shades of Oleylamine*<sup>8</sup> as much less conducive to the “sphere-to-rod” transformation than the 7:3 one, due to the too limited “reservoir” of oleylamine “fuel”. The XPS spectra are given in Figure 6 (Co 2p), Figure 7 (Cl 2p, P 2s and P 2p) and Figure 8 (N 1s). One major observation is the fact that phosphorus is back in the spotlight, and the decomposition of its core level spectra will show that it forms a compound with cobalt.

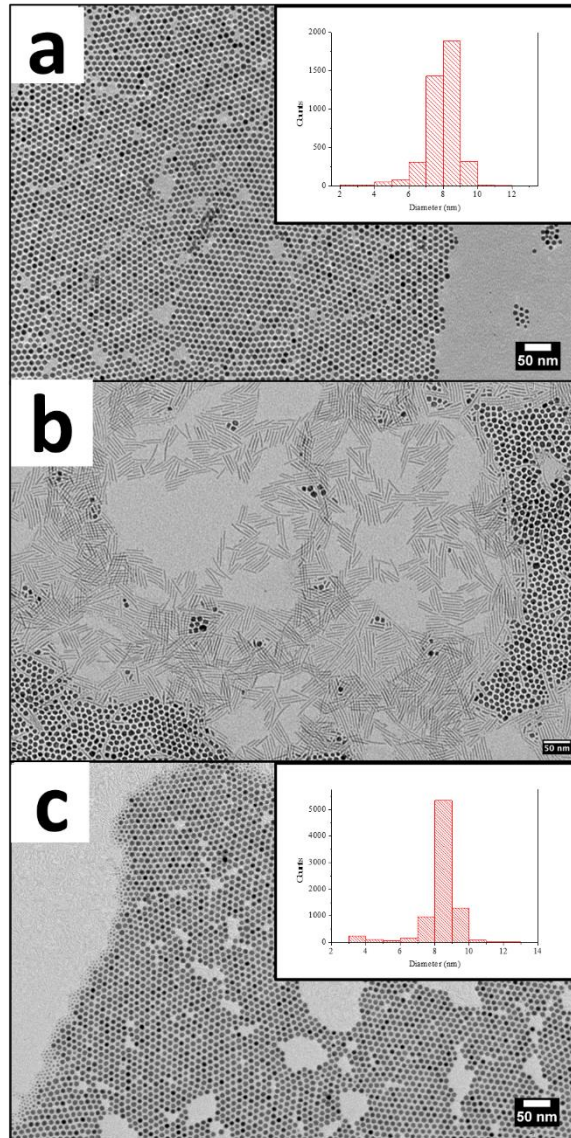


*Figure 5. TEM micrographs and particle size distribution of concentrated cobalt nanoparticle films synthesized in mixtures of 7:3 TD:OAm (a and b) and 9:1 TD/OAm (c). The reaction time in (a) and (c) is 60 min (temperature ramp up to 190°C). The diameter of the spheres is  $7.9 \pm 1$  nm and  $8.3 \pm 1.2$  nm in (a) and (c), respectively. In (b), the overall reaction time is 600 min (60 min for the temperature ramp plus 540 min at 190°C).*

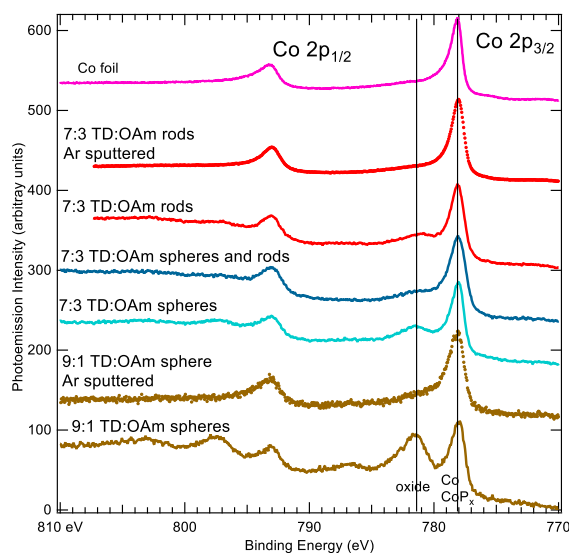


Figure 6. *Co 2p spectra of concentrated nanoparticle films (spheres, spheres-and-rods, and rods). BE are referenced to C 1s positioned at 285.0 eV. The clean Co foil BE is referenced to the Fermi level common to sample and analyzer. A monochromatized Al  $K\alpha$  source (1486.71 eV) was used.*

The  $Co\ 2p_{3/2}$  spectra of the nanoparticles present two structures. The one at  $\sim 778$  eV corresponds to metallic cobalt (the clean Co foil BE referenced to Fermi level is 778.1 eV, see Figure 6) or to cobalt phosphides, as previous studies<sup>22,23</sup> report virtually zero or small ( $\sim 0.2$

eV) shift in the Co 2p BE of CoP and Co<sub>2</sub>P with respect to pure Co. In this regard, useful information will be provided by the phosphorus core-levels. The component at higher BE ~781.2 eV is coincidental with that of the Co(II) complex, but it seems more reasonable to attribute it to oxidized Co. *Pure* cobalt nanoplatelets grown from the Co(I)Cl(PPh<sub>3</sub>)<sub>3</sub> precursor in the hexadecylamine/lauric mixture acid under H<sub>2</sub> pressure also appear susceptible to oxidation, as evidenced by the Co 2p spectrum presented in ref <sup>2</sup>. The Co 2p<sub>3/2</sub> BE of bulk oxides reported in the literature are 780.0 eV for CoO,<sup>24</sup> 780.1 eV for CoOOH,<sup>24</sup> and 780.4<sup>24</sup>-780.7<sup>25</sup> eV for Co(OH)<sub>2</sub>. The O 1s spectrum of the 7:3 TD:OAm spheres (see Figure S9 of the SI) shows two components, one at 532.3 eV likely due to organic contamination<sup>26</sup> and one at 530.9 eV. The latter one is close to that of OHs in Co(OH)<sub>2</sub> (531.07 eV<sup>24</sup>). Therefore, the surface oxide may be hydrated.

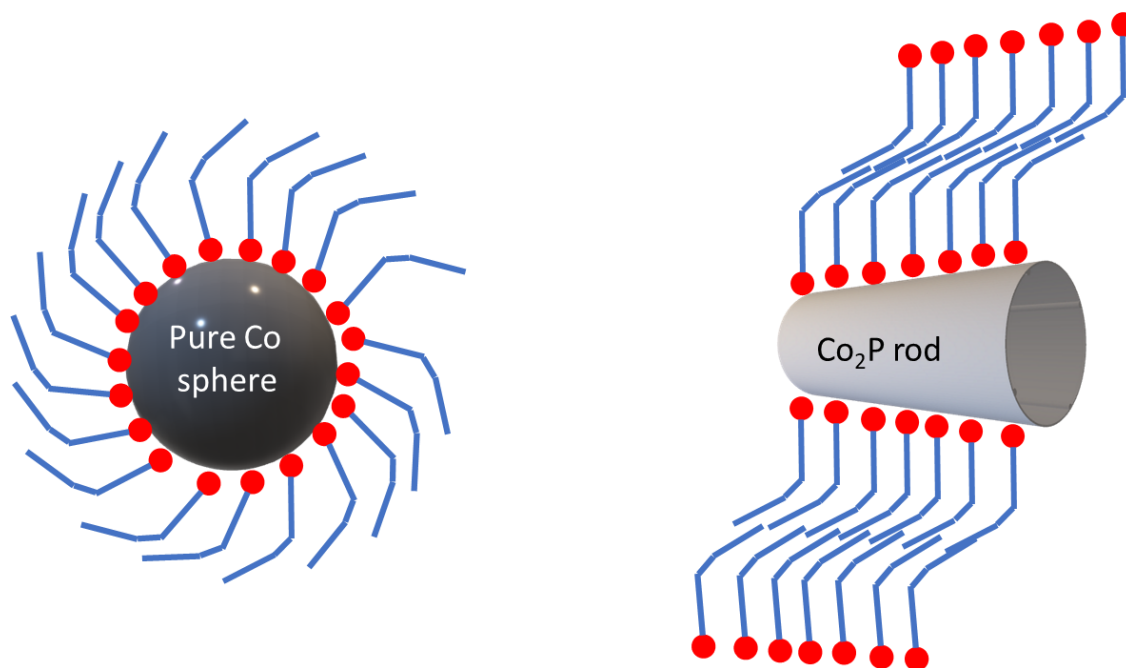
The  $\frac{I_{Co\ 3p}^{norm}}{I_{Co\ 2p}^{norm}}$  ratio (Figure S2 of the SI) always strongly deviates from 1, which is expected for a highly heterogeneous system consisting in nanoparticles dressed by one or more layers of OAm.

The fact that the  $\frac{I_{Co\ 3p}^{norm}}{I_{Co\ 2p}^{norm}}$  ratio of the 9:1 and 7:3 TD:OAm spheres is 2±0.2, means that the spheres are covered by one overlayer of OAm (the lowest KE Co 2p electrons are more inelastically scattered in OAm than the fastest Co 3p ones, see Figure S1). In the SI, section S7 we present a model of cubic-shaped particles (to ease the calculation) coated with one or two layers of OAm. When the particle is greater than 6 nm, which is the case for the 9:1 and 7:3 TD:OAm spheres, the adsorption of one OAm monolayer (2.33 nm) yields a calculated  $\frac{I_{Co\ 3p}^{norm}}{I_{Co\ 2p}^{norm}}$  ratio of 1.6

(Figure S11), in good accord with experiment. The experimental  $\frac{I_{Co\ 3p}^{norm}}{I_{Co\ 2p}^{norm}}$  ratio reaches 2.3 for the “spheres and rods” and “rods” films (Figure S2). Rods of diameter 2.7±0.3 nm and length 32.6±12 nm lie flat on the surface. Thus, only the diameter matters. Figure S11 in the SI shows

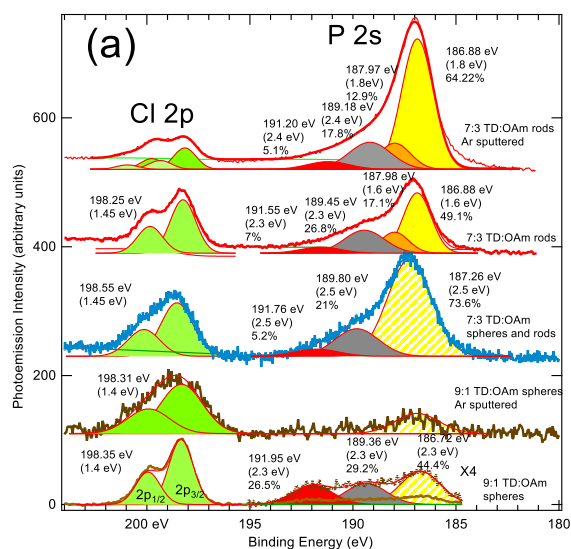
that for a characteristic dimension of  $\sim 3$  nm, *two layers* of OAm lead to a calculated  $\frac{I_{Co\ 3p}^{norm}}{I_{Co\ 2p}^{norm}}$  ratio in accord with experiment.

The intensity ratio  $\frac{I_{C\ 1s}^{norm}}{I_{N\ 1s}^{norm}}$  (Figure S5 of the SI) also give information on the way OAm bonds to the nanoparticle. For the spheres  $\frac{I_{C\ 1s}^{norm}}{I_{N\ 1s}^{norm}}$  is  $\sim 40$ , a value close to that found for a pure OAm film,  $\sim 38$ . Spheres are coated with one OAm layer. The amine head is in contact with the nanoparticle surface and the carbon tail outwards, as in the pure OAm film. In contrast,  $\frac{I_{C\ 1s}^{norm}}{I_{N\ 1s}^{norm}}$  is only  $\sim 8$  for the rods that are coated with two layers. Qualitatively, this can be explained as follows: the amine head of the first OAm layer touches the particle surface, but the second layer is oriented in the opposite direction, with the amine head pointing outward. Naturally, the relative nitrogen signal will increase with respect to the sphere case. This double-layer capping of the rods may result from their particular growth mode in a lamellar structure.<sup>27</sup> The sphere and the rod coatings are depicted in Scheme 2.



**Scheme 2.** Single and double OAm layer capping for the spheres and rods, respectively.

For the “9:1 TD:OAm spheres” and for the “rods”, a “mild” 1 keV Ar-bombardment of 5 min leads to the elimination of the OAm overlayer, as the experimental  $\frac{I_{Co\ 3p}^{norm}}{I_{Co\ 2p}^{norm}}$  ratio is now equal to  $\sim 1$  (Figure S2). Note also that the oxide(hydroxide) component in the Co 2p spectrum disappears after Ar sputtering which shows that oxidation only concerns the external part of the NPs.



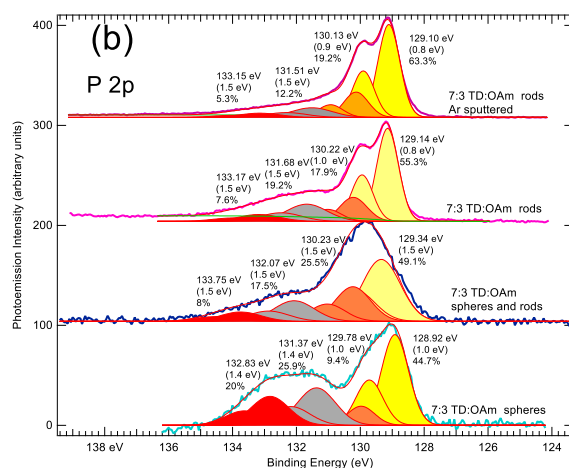
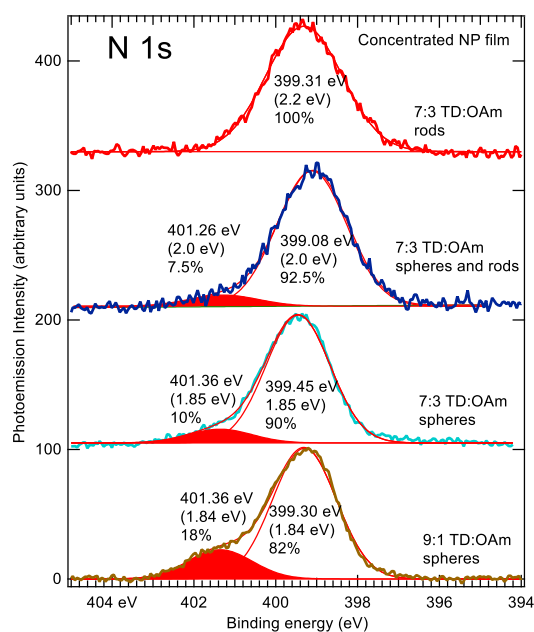


Figure 7. (a) Cl 2p-P 2s spectral region and (b) P 2p spectra of concentrated nanoparticles films (spheres, spheres-and-rods, and rods) prepared from centrifugated TD:OAm solutions (the ratio is indicated). BE are referenced to C 1s positioned at 285.0 eV. A monochromatized Al  $K_{\alpha}$  source (1486.71 eV) was used. The experimental curves are fitted with sums of Gaussians (red solid curves), whose BE positions of Cl 2p<sub>3/2</sub>, P 2s and P 2p<sub>3/2</sub> components, FWHMs (between parentheses) and spectral weights (%) are also given.



*Figure 8.* N 1s spectra of concentrated nanoparticles films (spheres, spheres-and-rods, and rods) prepared from centrifugated TD:OAm solutions (the ratio is indicated). BE are referenced to C 1s positioned at 285.0 eV. A monochromatized Al  $K_{\alpha}$  source (1486.71 eV) was used. The experimental curves are fitted with sums of Gaussians (red solid curves), whose BE positions, FWHMs (between parentheses) and spectral weights are also given.

The Cl 2p spectra of the concentrated nanoparticle films are given in Figure 7(a). The Cl 2p<sub>3/2</sub> BE is  $\sim 198.35 \pm 0.15$  eV, a value characteristic of the Cl<sup>-</sup> anion (see above). It can form a salt with ammonium species, or be part of a cobalt hydroxyl chloride compound (e.g. in Co<sub>2</sub>(OH)<sub>3</sub>Cl, a solid solution of CoCl<sub>2</sub> and Co(OH)<sub>2</sub>,<sup>28</sup> or as a counter ion within positively charged Co(OH)<sub>2-x</sub> layers<sup>29</sup>). The  $\frac{I_{\text{Cl } 2p}^{\text{norm}}}{I_{\text{Co } 2p}^{\text{norm}}}$  and  $\frac{I_{\text{Cl } 2p}^{\text{norm}}}{I_{\text{Co } 3p}^{\text{norm}}}$  ratios (see Table S4) strongly decrease after Ar sputtering, which shows chloride ions are located at the particle periphery.

The P 2s and P 2p spectra shown in Figure 7 (a) and (b), respectively, give key information to understand the nanoparticle synthesis reactions. The Gaussian fitting of the P 2s spectrum features a component at  $186.9 \pm 0.2$  eV, whose BE is lower than that of pure phosphorus ( $\sim 188$  eV<sup>18</sup>). This suggests the formation of a metal phosphide (P<sup>δ-</sup>). *It is observed for all types of washed nanoparticle films, spheres and rods alike.* In the “rods” film, the energy resolution is good enough to make it necessary to insert an orange-shaded component to the left of the “phosphide” peak at  $\sim 188$  eV we attribute to pure phosphorus. For its part, the peak at  $189.6 \pm 0.2$  eV can be attributed to “intact” PPh<sub>3</sub> molecules (PPh<sub>3</sub> free or liganded to Co(II) is found in the  $189.0 \pm 0.2$  eV range, see Figure 3(a). A sizeable (26% of the spectral weight) red-shaded peak at a BE of 191.9 eV is observed for the “9:1 TD:OAm spheres”. It can result from “oxidized PPh<sub>3</sub>” (e.g. triphenylphosphine oxide) or from a PO<sub>x</sub> compound resulting from the surface oxidation of a CoP<sub>x</sub> compound (see also below the discussion of the P 2p spectra). Ar-sputtering tends to increase the phosphide spectral weight, by eliminating PPh<sub>3</sub> and “oxidized PPh<sub>3</sub>”/PO<sub>x</sub> species which are therefore probably present on the surface of the particle. The examination of the narrower and more extensively documented P 2p spectra (Figure 7(b)) provides further insights into the chemical states of phosphorus. The P 2p spectrum of the “rods” is particularly well-resolved, considering the spin-orbit splitting of 0.8 eV. All four spectra are decomposed in the same consistent manner as the P 2s spectra. The yellow-shaded doublet at  $129.1 \pm 0.2$  eV

undoubtedly originates from a phosphorus-cobalt alloy. Indeed the P 2p<sub>3/2</sub> BE is reported at 129.1 eV for nanometer-size CoP and Co<sub>2</sub>P particles<sup>30</sup> (129.5 eV for bulk CoP<sup>22</sup>). Another orange-shaded doublet at 130.2 ± 0.2 eV is well-visible in the most resolved spectrum, specifically that of the rods. As mentioned earlier, pure phosphorus is a possible candidate, considering the average P 2p<sub>3/2</sub> BE of 130.09 ± 0.34 eV based on thirteen BEs from the NIST database.<sup>18</sup> The grey-shaded doublet at ~131.4 eV is attributed to intact PPh<sub>3</sub>. Finally, a particularly intense, red-shaded component at 132.8 eV is observed in the spectrum of the “7:3 TD:OAm spheres” film. This BE matches that of the “oxidized PPh<sub>3</sub>” species, in the Co(I) powder (triphenylphosphine oxide, triphenyl phosphite). The spectral weight of the oxidized PPh<sub>3</sub> component is significantly reduced in the rods’ spectrum compared to the spheres’ one. After Ar-sputtering of the “7:3 TD:OAm rods” film, the contribution of PPh<sub>3</sub> and “oxidized PPh<sub>3</sub>” components diminishes, corroborating the trend already observed for the P 2s spectra (these are surface species). Finally, when comparing the P 2p (and P 2s) spectra of the “spheres” and “rods”, it becomes evident that the weight of phosphide is considerably greater in the rods than in the spheres.

The kinetic study has shown that spheres grown during times of one hour (and with a diameter of ~8 nm) are pure cobalt (there is no P signal in the aliquot depth probed by XPS). As a result, for films composed of washed and centrifuged spherical particles with the same growth time and diameter (Figure 5 (a,c)), the spheres are also composed of pure cobalt. Consequently, the XPS phosphorus signal in the concentrated films must originate from separate cobalt phosphide particles that elude TEM detection, likely due to their small size. These phosphide particles are necessarily formed independently from the spheres, within the “sink” of organophosphorus ligands mentioned earlier. The  $\frac{I_{P\ 2p}^{norm}}{I_{Co\ 3p}^{norm}}$  ratio is ~0.17 for the sputtered “9:1 TD:OAm spheres” (Table S4 of the SI). A value less than 0.5 is consistent with a mixture of pure Co spheres and phosphide particles with a Co<sub>2</sub>P or CoP stoichiometry.

The situation is much simpler for the nanorods, which are the end-product of a series of chemical reactions. Consider the nanorods cleaned with Ar sputtering, with an experimental ratio  $\frac{I_{Co\ 3p}^{norm}}{I_{Co\ 2p}^{norm}}$  of  $\sim 1$ . In this case,  $\frac{[P]}{[Co]}$  is found equal to  $0.8 \pm 0.1$ . The P 2p spectrum in Figure 7 (b) shows that the phosphide component at 129.2 eV is 63% of the whole spectrum. Therefore, the  $\frac{[P\ in\ phosphide]}{[Co]}$  ratio is  $\sim 0.5 (\pm 0.07)$ . In the XPS probed layers, the stoichiometry is close to  $Co_2P$ . This means that the rods are heavily phosphidized as the  $\lambda_s$  of P 2p and Co 3p photoelectrons (in  $CoP_x$  and Co) compare with the diameter of the rods ( $2.7 \pm 0.3$  nm). There is no significant pure cobalt core (a microscopy study will confirm it, see below). Finally, note that the resistance to oxidation is different for spheres and rods. Figure 6 shows that cobalt is significantly oxidized on pure cobalt spheres and much less on rods that are phosphidized. It suffices to admit that  $CoP_x$  is less prone to oxidation than bare metallic Co.

The N 1s spectra of the concentrated particle films are given in Figure 8. For the three samples, the main component is at  $399.2 \pm 0.1$  eV. The formation of an aldimine species suggested by the sphere-to-rod transition model in “*Five Shades*” (reaction R2) should lead to a component at 398.4 eV (clearly distinguished from the amine peak in the case of PtZn nanoparticles dressed in OAm, see ref<sup>31</sup>). Given the standard deviations, the chemical shift of the N 1s peak centroid with respect to the “amine” OAm BE at  $399.6 \pm 0.3$  eV in the TD:OAM mixture (see SI Figure S4) is too small to be meaningfully attributed to an aldimine contribution. The absence of the aldimine can be rationalized considering that the amine binds more strongly to the cobalt metal surface than the aldimine. Indeed, the more stable calculated adsorption energies of  $CH_3CH=NH$  and  $CH_3CH_2NH_2$  on the Co(0001) facet are  $-1.98$  eV and  $-2.61$  eV, respectively.<sup>32</sup> Thus the aldimine should be displaced by OAm at the cobalt/solution interface, and then washed out during the preparation of the concentrated particle film. For its part, the red-shaded component at 401.4 eV in the spectrum of the 9:1 and 7:3 TD:OAm sphere sample,

with spectral weights of ~20% and 10%, respectively, can be attributed to the ammonium species<sup>2</sup> (R-CH<sub>2</sub>NH<sub>3</sub><sup>+</sup>). This confirms one crucial tenet of the model depicted in *The Five Shades*<sup>8</sup> (reaction R5).

### 3.4 Crystallographic data revisited: nanorods are effectively made of Co<sub>2</sub>P

The information provided by XPS (CoP<sub>x</sub> formation) allowed us to take a fresh look at the crystallographic data presented in our earlier works. In Meziane et al.<sup>6</sup> the electron diffraction patterns were indeed indexed considering a distorted form of *hcp* metallic cobalt. However, the attribution of an intense diffraction ring (with an interplanar distance of ~0.174 nm) remained elusive. Actually, all difficulties vanish if one admits, in light of the XPS results, that the composition of the nanorods is Co<sub>2</sub>P. Bulk Co<sub>2</sub>P has the orthorhombic anti-PbCl<sub>2</sub> structure, and its parameters have been reported to be  $a = 0.3513 \text{ \AA}$ ,  $b = 0.5646 \text{ \AA}$ , and  $c = 0.6608 \text{ \AA}$  by Rundqvist.<sup>33</sup> We show in Figure 9 (a) the TEM image of nanorods, whose electron diffraction pattern is given in Figure 9 (b). The diffraction rings are indexed with the Co<sub>2</sub>P interplanar distances reported in

Table 1. In particular, the strong ring at 0.175 nm, which is difficult to interpret assuming that rods are made of pure cobalt, corresponds to the (200) reflection of Co<sub>2</sub>P. Intensities and interplanar distances are identical to those found by Murray's group<sup>34</sup> who produced Co<sub>2</sub>P particles by a different method (using Co(II) acetate in a mixture of trioctylphosphine oxide and oleic acid). The Fourier transform of the HRTEM image of a nanorod shows that the growth axis is along  $\langle 200 \rangle$ , a feature also observed in ref<sup>34</sup>.

Bulk Co<sub>2</sub>P exhibits paramagnetic properties above 10 K and antiferromagnetic behavior below this temperature.<sup>35</sup> Consequently, Co<sub>2</sub>P nanorods are not suitable for use in magnetic devices. However, their synthesis should not be viewed as a setback, since Co<sub>2</sub>P nanoparticles

show significant potential in the field of electrocatalytic hydrogen production through water splitting<sup>30,34,36,37</sup>

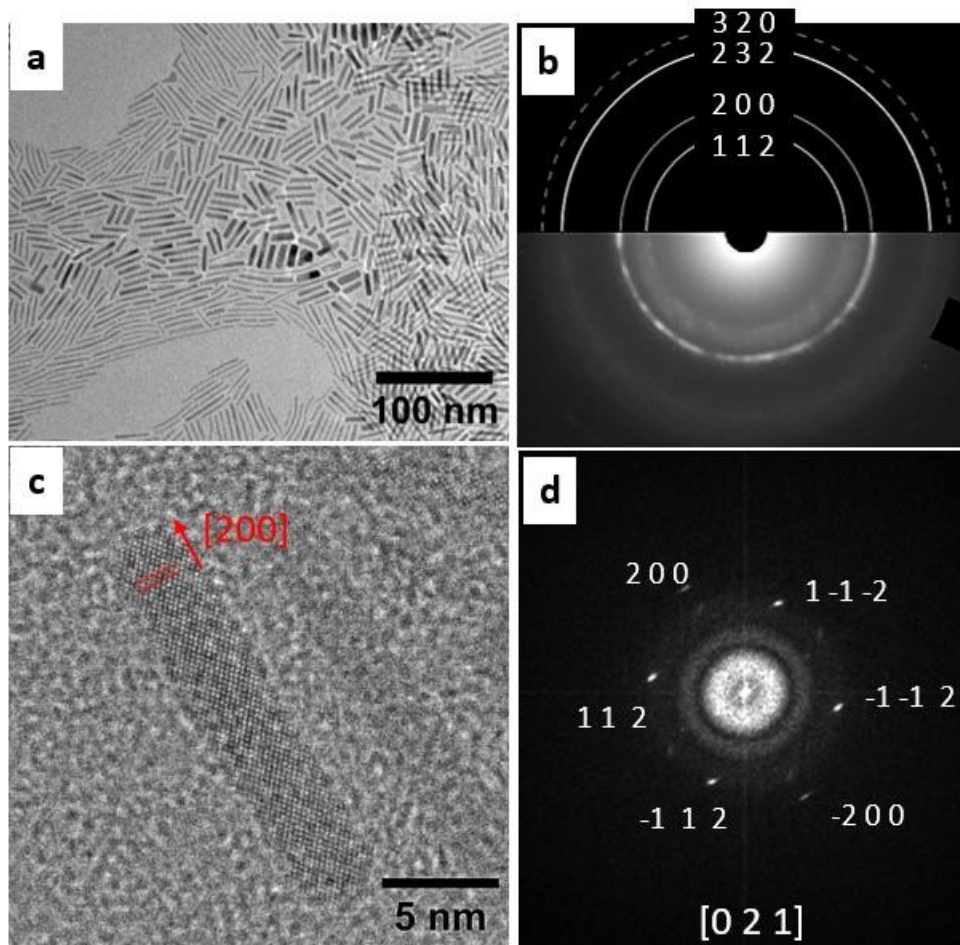


Figure 9. (a) TEM of the  $\text{Co}_2\text{P}$  nanorods, (b) the electron diffraction pattern of the nanorods presented in (a). Interplanar distances are indexed with the following reflections of  $\text{Co}_2\text{P}$  (312), (232), (200), and (112) (see Table 1). (c) high resolution image of a nanorod. (d) the Fourier transform of image (c), emphasizing the (200) and (112) reflections.

Co <sub>2</sub> P Plane	Co <sub>2</sub> P interplane Distances (nm)
(312)	0.1067
(232)	0.1197
(200)	0.1756
(112)	0.2214

*Table 1. Indexed reflections and corresponding interplanar distances of the Co<sub>2</sub>P nanorods.*

### 3.5 Should we propose a new narrative?

In the final stage of the “kinetic” study (171°C –190°C) leading to the growth of spherical cobalt particles the Co 2p spectra clearly show the formation of metallic cobalt (in agreement with structural tools observation<sup>8</sup>) and of a Co(II) complex. Therefore we see nothing fundamentally incompatible with the “simple” disproportionation reaction hypothesis.<sup>6-8</sup> However, the observation of a phosphide component in the P 2s and P 2p core-levels of the concentrated nanoparticle films is a major contribution of XPS to the understanding of the particle growth mechanism, as cobalt phosphidation was not considered in the previous reports.<sup>6-8</sup>

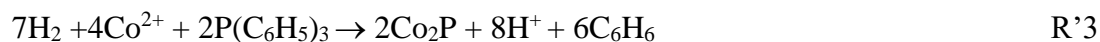
Various mechanisms for the phosphidation of cobalt can be hypothesized. In one such mechanism, cobalt particles form first, after which they interact with organophosphorus molecules. In this scenario, the cobalt particles are transformed into CoP<sub>x</sub> from the external surface where the organophosphorus molecule decomposes, thereby releasing phosphorus

atoms.<sup>38</sup> Then, as Co<sub>2</sub>P is impermeable to Co and P diffusion, once a critical thickness is reached hollow spheres (Co comes from inside) are formed. This mechanism does not apply here for two reasons: first, spheres are made of pure cobalt with no signs of any surface phosphidation, and, second, nanorods are the end-product, not hollow spheres.

Therefore, to elucidate the formation of Co<sub>2</sub>P rods in conjunction with the etching of Co spheres, we need to explore other mechanisms than the direct reaction of phosphorus at the surface of the preformed pure Co particles. We shall maintain the general framework outlined in "*Five Shades of Oleylamine*"<sup>8</sup> to describe the transition from nanospheres to nanorods, but this time organophosphorus ligands play a role. *Co-P nuclei should form in places (nanoreactors, see scheme 1) where both Co<sup>2+</sup> and organophosphorus ligands are both present.*

The starting point of the nanorod growth is a situation where pure ~9 nm Co metal spheres coexist with the Co(II)Cl<sub>2</sub> complex. However, this situation is unstable, as OAm dissociates on the surface of cobalt spheres according to reactions R2, generating H<sub>2</sub>. We adhere to the crucial tenet of *The Five Shades of Oleylamine*: H<sub>2</sub> reduces the Co(II) complex, yielding zero-valent Co(0) and HCl (in turn HCl etches the pure cobalt sphere, thereby regenerating the Co(II) complex). However, H<sub>2</sub> reaction with the organophosphorus ligands also leads to formation of atomic P, as the final product is Co<sub>2</sub>P. These combined reactions (sphere etching and Co and P release) indeed prompt the replacement of Co spheres with nanorods, but these nanorods have a Co<sub>2</sub>P stoichiometry. Necessarily, Co<sup>2+</sup> and organophosphorus ligands should be present in the same "nanoreactor", likely resulting from a structuration of OAm.

Therefore, the primary revision to the sphere-to-rod transition model outlined in "*The Five Shades of Oleylamine*" involves modifying the reductive reaction R3 to produce Co<sub>2</sub>P instead of Co. When considering triphenylphosphine as the phosphorus source, the overall reaction can be represented as follows:



The detection of benzene (and possibly of biphenyl) could confirm this scheme.

#### 4. Conclusions

This XPS study illuminates further insight into the growth mechanism of cobalt nanoparticles in oleylamine starting from a rather unusual precursor, a Co(I) complex. It demonstrates that a partial reevaluation of the framework presented in *The five shades of oleylamine*<sup>8</sup> is needed. Although oleylamine continues to play a pivotal role in the synthesis as source of hydrogen and a templating agent, XPS unveils the significant involvement of organophosphorus ligands, notably triphenylphosphine and, possibly its oxidized form. XPS analysis of the precursor powder suggests that the latter molecule contributes a significant part of the overall phosphorus content, at least at the surface of the grains probed by the spectroscopy, as “bulk” analysis tools point to pure triphenylphosphine.

In analyzing changes in the tetradecane:oleylamine precursor solution with time and temperature using the aliquot method, XPS supports the occurrence of the Co(I) disproportionation reaction to Co(II) and Co(0) during the “sphere growth stage”. It also shows that the organophosphorus ligands expelled from the XPS probed surface layers of the aliquots are replaced by oleylamine and confirms that spheres are made of pure cobalt. Nonetheless, there remains a possibility of phosphide particle formation in deeper layers that remain beyond the probing capacity of XPS.

Subsequent XPS examination of washed, centrifugated nanoparticle films provides evidence for the presence of cobalt phosphidation across all synthesis stages. Phosphide formation increases during the “sphere-to-rod” transition, with an XPS Co/P atomic ratio reaching ~ 2 for the nanorods only films.

This unexpected revelation warrants the reevaluation of previously published data. Electron diffraction patterns, reinterpreted in light of these findings, confirm beyond doubt that rods are composed of dicobalt phosphide, contradicting earlier assumptions of pure cobalt composition made in the *The Five Shades of Oleylamine*. Consequently, the mechanisms describing the sphere-to-rod transition must also be reassessed. The dissociation of oleylamine (OAm) – inducing the release of H<sub>2</sub> and the subsequent reduction of Co(II) to metallic cobalt – remains a central feature, similar to the preceding model. However, as the final product is a metal phosphide, not a pure metal, organophosphorus molecules must dissociate and release P atoms. We suggest a reaction scheme where H<sub>2</sub> is also instrumental in the decomposition of the organophosphorus ligand, incorporating it within the conceptual model outlined in *The Five Shades of Oleylamine*.

Lastly, the novel synthesis, which produces Co<sub>2</sub>P nanorods at a relatively low reaction temperature (~190°C), compared to the standard process (~330°C), is a notable finding, given the promising applications of this material, particularly in electrocatalytic water splitting.

## SUPPORTING INFORMATION

The Supporting Information is available free of charge via the Internet at <http://pubs.acs.org>.

Figure S1. (TPP-2M  $\lambda$  values in bulk cobalt, bulk Co<sub>2</sub>P, bulk CoP and OAm/TD in the 706-1436 eV energy interval.

Figure S2.  $\frac{I_{\text{Co } 3p}^{\text{norm}}}{I_{\text{Co } 2p}^{\text{norm}}}$  for the various samples examined in this study.

Figure S3. C 1s, P 2p and Co 2p spectra of HCo(P(OPh)<sub>3</sub>)<sub>4</sub> and HCo(PhP(OEt)<sub>2</sub>)<sub>4</sub>.

Figure S4. N 1s core-levels of the precursor-containing 7:3 TD:OAm mixture aliquots.

Figure S5.  $\frac{I_{\text{C } 1s}^{\text{norm}}}{I_{\text{N } 1s}^{\text{norm}}}$  for the 7:3 TD:OAm mixture and for the concentrated washed particle films.

Figure S7. Co 2p spectra of concentrated nanoparticles (spheres) grown at room temperature in THF.

Figure S8. Cl 2p and P 2s spectra of concentrated nanoparticles grown in THF at room temperature.

Figure S9. O 1s spectra of concentrated nanoparticles films (spheres, spheres-and-rods, and rods) prepared from centrifugated TD:OAm solutions.

Figure S10. Top view of the nanoparticle packing model.

Figure S11. The ratio  $\frac{I_{Co\ 3p}^{norm}}{I_{Co\ 2p}^{norm}}$  as a function of nanoparticle distance and OAm dressing.

Table S1. Raw spectral intensities  $I_{X\ CL}$  in (counts per second) $\times eV$

Table S2. Acquisition time  $\tau$  (dwell-time  $\times$  number of scans) and  $\frac{1}{\sqrt{\tau \times I_{X\ CL}}}$  value

Table S3. Sensitivity factor  $Q_{X\ CL}$ .

Table S4. Useful  $\frac{I_{X\ CL}^{norm}}{I_{Y\ CL}^{norm}}$  ratios.

## AUTHOR CONTRIBUTION

Rabah Benbalagh: Methodology (XPS), Investigation (XPS), Validation (XPS), Review and Editing.

François Rochet: Conceptualization (XPS), Methodology (XPS), Validation (XPS), Writing – original draft.

Arthur Moisset: Preparation (Co(I)Cl(PPh<sub>3</sub>)<sub>3</sub> precursor and growth of nanoparticles), Methodology (Aliquots).

Alexandre Sodreau: Preparation (Co(I)Cl(PPh<sub>3</sub>)<sub>3</sub> precursor and growth of nanoparticles).

Cassandre Bories: Preparation (Hydrido-cobalt(I) complexes).

Caroline Salzemann: Conceptualization (Particle Growth), Methodology (TEM, Preparation), Investigation (TEM), Validation (TEM). Review and Editing

Christophe Petit: Conceptualization (Particle Growth), Methodology (TEM), Investigation (TEM), Validation, Fund Raising and Scientific Coordination (ANR NUMEN). Review and Editing.

Marc Petit: Conceptualization (Precursor Preparation, Particle Growth), Methodology (Characterization), Investigation, Validation. Review and Editing.

All authors have given approval to the final version of the manuscript.

## **ACKNOWLEDGEMENTS**

This work was financially supported by Sorbonne Université, CNRS, and the French National Research Agency (ANR) in the framework of the program entitled “Nucleation, growth and reactivity of MEtallic and bimetallic Nanocrystals” (NUMEN) under reference ANR- 17-CE09-0037. The upgrade of the XPS platform (Institut Parisien de Chimie Physique et Théorique) received support from the ANR-NUMEN.

## **CORRESPONDING AUTHORS**

François Rochet E-mail : [francois.rochet@sorbonne-universite.fr](mailto:francois.rochet@sorbonne-universite.fr);

**REFERENCES**

- (1) De Vrieze, J. E.; Bremmer, G. M.; Aly, M.; Navarro, V.; Thybaut, J. W.; Kooyman, P. J.; Saeys, M. Shape of Cobalt and Platinum Nanoparticles Under a CO Atmosphere: A Combined In Situ TEM and Computational Catalysis Study. *ACS Catal.* **2019**, *9* (8), 7449–7456. <https://doi.org/10.1021/acscatal.9b01840>.
- (2) Kaźmierczak, K.; Yi, D.; Jaud, A.; Fazzini, P.-F.; Estrader, M.; Viau, G.; Decorse, P.; Piquemal, J.-Y.; Michel, C.; Besson, M. et al. *J. Phys. Chem. C* **2021**, *125* (14), 7711–7720. <https://doi.org/10.1021/acs.jpcc.1c01388>.
- (3) Gambardella, P.; Rusponi, S.; Veronese, M.; Dhési, S. S.; Grazioli, C.; Dallmeyer, A.; Cabria, I.; Zeller, R.; Dederichs, P. H.; Kern, K. et al. Giant Magnetic Anisotropy of Single Cobalt Atoms and Nanoparticles. *Science (80-. )*. **2003**, *300* (5622), 1130–1133. <https://doi.org/10.1126/science.1082857>.
- (4) Mourdikoudis, S.; Liz-Marzán, L. M. Oleylamine in Nanoparticle Synthesis. *Chemistry of Materials*. American Chemical Society 2013, pp 1465–1476. <https://doi.org/10.1021/cm4000476>.
- (5) Diana, F. S.; Lee, S.-H.; Petroff, P. M.; Kramer, E. J. Fabrication of Hcp-Co Nanocrystals via Rapid Pyrolysis in Inverse PS- b -PVP Micelles and Thermal Annealing. *Nano Lett.* **2003**, *3* (7), 891–895. <https://doi.org/10.1021/nl034262l>.
- (6) Meziane, L.; Salzemann, C.; Aubert, C.; Gérard, H.; Petit, C.; Petit, M. Hcp Cobalt Nanocrystals with High Magnetic Anisotropy Prepared by Easy One-Pot Synthesis. *Nanoscale* **2016**, *8* (44), 18640–18645. <https://doi.org/10.1039/C6NR05792F>.
- (7) Vivien, A.; Guillaumont, M.; Meziane, L.; Salzemann, C.; Aubert, C.; Halbert, S.; Gérard, H.; Petit, M.; Petit, C. Role of Oleylamine Revisited: An Original Disproportionation Route to Monodispersed Cobalt and Nickel Nanocrystals. *Chem. Mater.* **2019**, *31* (3), 960–968. <https://doi.org/10.1021/acs.chemmater.8b04435>.

- (8) Moisset, A.; Sodreau, A.; Vivien, A.; Salzemann, C.; Andrezza, P.; Giorgio, S.; Petit, M.; Petit, C. The Five Shades of Oleylamine in a Morphological Transition of Cobalt Nanospheres to Nanorods. *Nanoscale* **2021**, *13* (25), 11289–11297. <https://doi.org/10.1039/D1NR01502H>.
- (9) Guillaumont, M.; Fourré, I.; Pilmé, J.; Halbert, S.; Gérard, H. Triggering Electron Transfer in Co(I) Dimers: Computational Evidences for a Reversible Disproportionation Mechanism. *ChemPhysChem* **2021**, *22* (8), 788–795. <https://doi.org/10.1002/cphc.202000965>.
- (10) Egelhoff, W. F. Core-Level Binding-Energy Shifts at Surfaces and in Solids. *Surf. Sci. Rep.* **1987**, *6* (6–8), 253–415. [https://doi.org/10.1016/0167-5729\(87\)90007-0](https://doi.org/10.1016/0167-5729(87)90007-0).
- (11) Briggs, D.; Beamson, G. Primary and Secondary Oxygen-Induced C1s Binding Energy Shifts in x-Ray Photoelectron Spectroscopy of Polymers. *Anal. Chem.* **1992**, *64* (15), 1729–1736. <https://doi.org/10.1021/ac00039a018>.
- (12) Tong, Y.; Berdiyrov, G. R.; Sinopoli, A.; Madjet, M. E.; Esaulov, V. A.; Hamoudi, H. An Estimation on the Mechanical Stabilities of SAMs by Low Energy Ar<sup>+</sup> Cluster Ion Collision. *Sci. Rep.* **2021**, *11* (1), 12772. <https://doi.org/10.1038/s41598-021-92077-3>.
- (13) Weinhardt, L.; Blum, M.; Fuchs, O.; Pookpanratana, S.; George, K.; Cole, B.; Marsen, B.; Gaillard, N.; Miller, E.; Ahn, K.-S.; Shet, S. et al. Soft X-Ray and Electron Spectroscopy to Determine the Electronic Structure of Materials for Photoelectrochemical Hydrogen Production. *J. Electron Spectros. Relat. Phenomena* **2013**, *190*, 106–112. <https://doi.org/10.1016/j.elspec.2012.11.015>.
- (14) Blackburn, J. R.; Nordberg, R.; Stevie, F.; Albridge, R. G.; Jones, M. M. Photoelectron Spectroscopy of Coordination Compounds. Triphenylphosphine and Its Complexes. *Inorg. Chem.* **1970**, *9* (10), 2374–2376. <https://doi.org/10.1021/ic50092a039>.
- (15) Yeh, J. J.; Lindau, I. Atomic Subshell Photoionization Cross Sections and Asymmetry Parameters:  $1 < Z < 103$ . *At. Data Nucl. Data Tables* **1985**, *32*, 1–155.
- (16) Krzystek, J.; Ozarowski, A.; Zvyagin, S. A.; Telser, J. High Spin Co(I): High-Frequency and -

- Field EPR Spectroscopy of  $\text{CoX}(\text{PPh}_3)_3$  ( $X = \text{Cl}, \text{Br}$ ). *Inorg. Chem.* **2012**, *51* (9), 4954–4964. <https://doi.org/10.1021/ic202185x>.
- (17) Mosaferi, M.; Selles, P.; Miteva, T.; Ferté, A.; Carniato, S. Interpretation of Shakeup Mechanisms in Copper L-Shell Photoelectron Spectra. *J. Phys. Chem. A* **2022**, *126* (30), 4902–4914. <https://doi.org/10.1021/acs.jpca.2c01870>.
- (18) NIST X-ray Photoelectron Spectroscopy Database, NIST Standard Reference Database Number 20, National Institute of Standards and Technology, Gaithersburg MD, 20899 (2000), DOI: <https://dx.doi.org/10.18434/T4T88K>, (retrieved 26-01-2024)
- (19) Halpern, J.; Pickard, A. L. Mechanism of the Tris(Triphenylphosphine)Platinum(0)-Catalyzed Oxidation of Triphenylphosphine. *Inorg. Chem.* **1970**, *9* (12), 2798–2800. <https://doi.org/10.1021/ic50094a040>.
- (20) Tereniak, S. J.; Landis, C. R.; Stahl, S. S. Are Phosphines Viable Ligands for Pd-Catalyzed Aerobic Oxidation Reactions? Contrasting Insights from a Survey of Six Reactions. *ACS Catal.* **2018**, *8* (4), 3708–3714. <https://doi.org/10.1021/acscatal.8b01009>.
- (21) Gorman, A. D.; Bailey, J. A.; Fey, N.; Young, T. A.; Sparkes, H. A.; Pringle, P. G. Inorganic Triphenylphosphine. *Angew. Chemie Int. Ed.* **2018**, *57* (48), 15802–15806. <https://doi.org/10.1002/anie.201810366>.
- (22) Grosvenor, A. P.; Wik, S. D.; Cavell, R. G.; Mar, A. Examination of the Bonding in Binary Transition-Metal Monophosphides  $\text{MP}$  ( $M = \text{Cr}, \text{Mn}, \text{Fe}, \text{Co}$ ) by X-Ray Photoelectron Spectroscopy. *Inorg. Chem.* **2005**, *44* (24), 8988–8998. <https://doi.org/10.1021/ic051004d>.
- (23) Nemoshalenko, V. V.; Didyk, V. V.; Krivitskii, V. P.; Senekevich, A. I. Investigation of the Atomic Charges in Iron, Cobalt and Nickel Phosphide. *Zh. Neorg. Khim.* **1983**, *28*, 2182.
- (24) Biesinger, M. C.; Payne, B. P.; Grosvenor, A. P.; Lau, L. W. M.; Gerson, A. R.; Smart, R. S. C. Resolving Surface Chemical States in XPS Analysis of First Row Transition Metals, Oxides and Hydroxides: Cr, Mn, Fe, Co and Ni. *Appl. Surf. Sci.* **2011**, *257* (7), 2717–2730.

- <https://doi.org/10.1016/j.apsusc.2010.10.051>.
- (25) Yang, J.; Liu, H.; Martens, W. N.; Frost, R. L. Synthesis and Characterization of Cobalt Hydroxide, Cobalt Oxyhydroxide, and Cobalt Oxide Nanodiscs. *J. Phys. Chem. C* **2010**, *114* (1), 111–119. <https://doi.org/10.1021/jp908548f>.
- (26) Briggs, D.; Beamson, G. XPS Studies of the Oxygen 1s and 2s Levels in a Wide Range of Functional Polymers. *Anal. Chem.* **1993**, *65* (11), 1517–1523. <https://doi.org/10.1021/ac00059a006>.
- (27) Lu, X.; Yavuz, M. S.; Tuan, H.-Y.; Korgel, B. A.; Xia, Y. Ultrathin Gold Nanowires Can Be Obtained by Reducing Polymeric Strands of Oleylamine–AuCl Complexes Formed via Auophilic Interaction. *J. Am. Chem. Soc.* **2008**, *130* (28), 8900–8901. <https://doi.org/10.1021/ja803343m>.
- (28) Zhang, Z.; Yin, L. Mn-Doped Co<sub>2</sub>(OH)<sub>3</sub>Cl Xerogels with 3D Interconnected Mesoporous Structures as Lithium Ion Battery Anodes with Improved Electrochemical Performance. *J. Mater. Chem. A* **2015**, *3* (34), 17659–17668. <https://doi.org/10.1039/C5TA03426D>.
- (29) Hu, Z.-A.; Xie, Y.-L.; Wang, Y.-X.; Xie, L.-J.; Fu, G.-R.; Jin, X.-Q.; Zhang, Z.-Y.; Yang, Y.-Y.; Wu, H.-Y. Synthesis of  $\alpha$ -Cobalt Hydroxides with Different Intercalated Anions and Effects of Intercalated Anions on Their Morphology, Basal Plane Spacing, and Capacitive Property. *J. Phys. Chem. C* **2009**, *113* (28), 12502–12508. <https://doi.org/10.1021/jp8106809>.
- (30) Pan, Y.; Lin, Y.; Chen, Y.; Liu, Y.; Liu, C. Cobalt Phosphide-Based Electrocatalysts: Synthesis and Phase Catalytic Activity Comparison for Hydrogen Evolution. *J. Mater. Chem. A* **2016**, *4* (13), 4745–4754. <https://doi.org/10.1039/C6TA00575F>.
- (31) Zakhtser, A.; Naitabdi, A.; Benbalagh, R.; Rochet, F.; Salzemann, C.; Petit, C.; Giorgio, S. Chemical Evolution of Pt–Zn Nanoalloys Dressed in Oleylamine. *ACS Nano* **2021**, *15* (3), 4018–4033. <https://doi.org/10.1021/acsnano.0c03366>.
- (32) Lozano-Blanco, G.; Adamczyk, A. J. Cobalt-Catalyzed Nitrile Hydrogenation: Insights into the

- Reaction Mechanism and Product Selectivity from DFT Analysis. *Surf. Sci.* **2019**, 688, 31–44.  
<https://doi.org/10.1016/j.susc.2019.06.003>.
- (33) Rundqvist, S.; Hede, A.; Rundqvist, S.; Varde, E.; Westin, G. The Structures of Co<sub>2</sub>P, Ru<sub>2</sub>P, and Related Phases. *Acta Chem. Scand.* **1960**, 14, 1961–1979.  
<https://doi.org/10.3891/acta.chem.scand.14-1961>.
- (34) Doan-Nguyen, V. V. T.; Zhang, S.; Trigg, E. B.; Agarwal, R.; Li, J.; Su, D.; Winey, K. I.; Murray, C. B. Synthesis and X-Ray Characterization of Cobalt Phosphide (Co<sub>2</sub>P) Nanorods for the Oxygen Reduction Reaction. *ACS Nano* **2015**, 9 (8), 8108–8115.  
<https://doi.org/10.1021/acsnano.5b02191>.
- (35) Ohta, S.; Onmayashiki, H. Antiferromagnetic Stability and Structural Trend of Transition-Metal Phosphides Containing Co. *Phys. B Condens. Matter* **1998**, 253 (3–4), 193–202.  
[https://doi.org/10.1016/S0921-4526\(98\)00381-0](https://doi.org/10.1016/S0921-4526(98)00381-0).
- (36) Dutta, A.; Samantara, A. K.; Dutta, S. K.; Jena, B. K.; Pradhan, N. Surface-Oxidized Dicobalt Phosphide Nanoneedles as a Nonprecious, Durable, and Efficient OER Catalyst. *ACS Energy Lett.* **2016**, 1 (1), 169–174. <https://doi.org/10.1021/acseenergylett.6b00144>.
- (37) Beltrán-Suito, R.; Menezes, P. W.; Driess, M. Amorphous Outperforms Crystalline Nanomaterials: Surface Modifications of Molecularly Derived CoP Electro(Pre)Catalysts for Efficient Water-Splitting. *J. Mater. Chem. A* **2019**, 7 (26), 15749–15756.  
<https://doi.org/10.1039/C9TA04583J>.
- (38) Ha, D.-H.; Moreau, L. M.; Bealing, C. R.; Zhang, H.; Hennig, R. G.; Robinson, R. D. The Structural Evolution and Diffusion during the Chemical Transformation from Cobalt to Cobalt Phosphide Nanoparticles. *J. Mater. Chem.* **2011**, 21 (31), 11498.  
<https://doi.org/10.1039/c1jm10337g>.

TOC

